

UNIVERSITY OF CRETE
SCHOOL OF SCIENCES AND ENGINEERING
DEPARTMENT OF MATERIALS SCIENCE & TECHNOLOGY



Development of Mesoporous
 $\text{Zn}_{1-x}\text{Cu}_x\text{S}$ Frameworks for Photocatalytic Water
Splitting Toward Hydrogen Production

Master thesis

IOANNIS DASKALAKIS

Supervisor: Prof. Gerasimos Armatas

HERAKLION 2019

ΠΑΝΕΠΙΣΤΗΜΙΟ ΚΡΗΤΗΣ
ΣΧΟΛΗ ΘΕΤΙΚΩΝ ΚΑΙ ΤΕΧΝΟΛΟΓΙΚΩΝ ΕΠΙΣΤΗΜΩΝ
ΤΜΗΜΑ ΕΠΙΣΤΗΜΗΣ ΚΑΙ ΤΕΧΝΟΛΟΓΙΑΣ ΥΛΙΚΩΝ



Ανάπτυξη Σύνθετων Μεσοπορώδων Πλεγμάτων
 $Zn_{1-x}Cu_xS$ για την Φωτοκαταλυτική Διάσπαση
του Νερού προς Παραγωγή Υδρογόνου

Μεταπτυχιακή Εργασία

Ιωάννης Δασκαλάκης

Επιβλέπων Καθηγητής: Γεράσιμος Αρματάς

ΗΡΑΚΛΕΙΟ 2019

ACKNOWLEDGMENTS

This master thesis has been accomplished at the department of Materials Science and Technology of the University of Crete.

First of all I want to thank my parents and my brother without them I wouldn't be the man I am, they have always trusted and supported me. I am grateful for all the patience and support all these years.

I would like to greatly thank my supervisor and advisor Professor Gerasimos Armatas for all the guidance and help he has shown to me. He has shared his knowledge on the field of Inorganic Synthetic Chemistry and Photocatalysis with me and he has been a person I look up too due to his achievements on the field of science.

I would like to thank and cherish all the members of the Laboratory of Advanced Materials Chemistry for the contribution and advices they have shared through helpful discussions; it was an honor and pleasure working with them in a friendly environment. I would like to thank personally Eirini Koutsouroubi, Evagelia skliri, Esmeralda Gotsi, Efi Mitaki, Konstantina Giovanopoulou and Giannis Tamiolakis for all the good memories we made together all these years. Giannis Vamvasakis, especially, has shared his experience on the field of Metal Chalcogenides and he has helped me a lot with various scientific and technical aspects during my experiments. It's a great bless to work with one of my best friends Stelios Papadogiorgakis, so I want to thank you for being there for me and support me. Also, I would like to thank all the former members of the Lab; Marios Savvakis, Ioannis Papadas, Georgia Velegraki, Yria Chalkiadaki and Alexandra Xilouri. My academic years at Crete were peaceful, joyful and you all worked as a catalyst for all these good moments.

ABSTRACT

As a potential answer to the global energy crisis and environmental pollution, the solar light hydrogen generation has recently attracted great attention. Currently, hydrogen is mainly being produced from fossil fuels or high-energy consumption processes, which are not environmentally friendly and economical methods. Since the first report by Fujishima and Honda on the photoelectrochemical water-splitting over a TiO_2 electrode, photocatalytic hydrogen production has become a promising approach for clean, economical, and environmentally viable production of solar fuels. This master thesis focuses on synthesis, structural characterization and energy applications of new 3D mesoporous frameworks consisting of connected Cu-doped ZnS nanocrystals ($\text{Zn}_{1-x}\text{Cu}_x\text{S}$; $x = 0.02, 0.05, 0.10$). In particular, we report the synthesis of high-surface-area mesoporous $\text{Zn}_{1-x}\text{Cu}_x\text{S}$ frameworks using a two-step chemical procedure that involves polymer-templated aggregating assembly of ZnS nanocrystals (~5 nm in size) and chemical transformation of ZnS constituents into $\text{Zn}_{1-x}\text{Cu}_x\text{S}$ heterostructures. The crystal structure, morphology and chemical composition of the prepared materials were characterized by powder X-ray diffraction (XRD), transmission electron microscopy (TEM), energy-dispersive X-ray spectroscopy (EDS), X-ray photoelectron spectroscopy (XPS) and N_2 porosimetry. Also, the electronic band structure of the $\text{Zn}_{1-x}\text{Cu}_x\text{S}$ heterostructures was investigated by UV-vis/NIR optical absorption and electrochemical impedance spectroscopy (EIS). Moreover, we highlight the impact of Cu doping on the photochemical behavior and visible-light photocatalytic H_2 production activity of the $\text{Zn}_{1-x}\text{Cu}_x\text{S}$ nanocrystal assemblies. An important aspect of this study is also the further improvement of the photocatalytic performance of $\text{Zn}_{1-x}\text{Cu}_x\text{S}$ catalysts by sulfur treatment.

ΠΕΡΙΛΗΨΗ

Τα τελευταία χρόνια, η χρήση του υδρογόνου ως εναλλακτική πηγή ενέργειας έχει προσελκύσει το ενδιαφέρον των ερευνητών. Επί του παρόντος, το υδρογόνο παράγεται κυρίως από ορυκτά καύσιμα ή άλλες διεργασίες που απαιτούν υψηλή κατανάλωση ενέργειας (π.χ. ηλεκτρόλυση νερού), οι οποίες δεν είναι φιλικές προς το περιβάλλον και οικονομικά συμφέρουσες. Έπειτα από την πρώτη αναφορά των Fujishima και Honda σχετικά με τη φωτοηλεκτροχημική διάσπαση νερού πάνω σε ηλεκτρόδιο TiO_2 , η φωτοκαταλυτική παραγωγή υδρογόνου έχει αποτελέσει μια πολλά υποσχόμενη μέθοδο για καθαρή, οικονομική και περιβαλλοντικά βιώσιμη παραγωγή ηλιακών καυσίμων. Αυτή η μεταπτυχιακή εργασία επικεντρώνεται στη σύνθεση, τον δομικό χαρακτηρισμό και τις ενεργειακές εφαρμογές νέων σύνθετων μεσοπορώδων υλικών που αποτελούνται από συνδεδεμένους νανοκρυστάλλους $\text{Zn}_{1-x}\text{Cu}_x\text{S}$ ($x = 0.02, 0.05, 0.10$). Συγκεκριμένα, αναφέρουμε τη σύνθεση σύνθετων πλεγμάτων $\text{Zn}_{1-x}\text{Cu}_x\text{S}$ υψηλής ειδικής επιφάνειας μέσω μιας χημικής διαδικασίας δύο σταδίων που περιλαμβάνει κατευθυνόμενη αυτο-συναρμολόγηση νανοκρυστάλλων ZnS (~5 nm σε μέγεθος) και, έπειτα, χημικό μετασχηματισμό των συστατικών ZnS σε ετεροδομές $\text{Zn}_{1-x}\text{Cu}_x\text{S}$. Η κρυσταλλική δομή, η μορφολογία και η χημική σύνθεση των παρασκευασθέντων υλικών χαρακτηρίστηκαν με περίθλαση ακτίνων-X (XRD), ηλεκτρονική μικροσκοπία διέλευσης (TEM), στοιχειακή μικροανάλυση ακτίνων-X (EDS), φασματοσκοπία φωτοηλεκτρονίων ακτίνων-X (XPS) και ποροσιμετρία N_2 . Οι οπτικές και ηλεκτρονιακές ιδιότητες των υλικών $\text{Zn}_{1-x}\text{Cu}_x\text{S}$ μελετήθηκαν με φασματοσκοπία οπτική απορρόφηση UV-vis/NIR και φασματοσκοπία ηλεκτροχημικής εμπέδησης (EIS). Επιπρόσθετα, η επίδραση των ιόντων Cu στη φωτοχημική συμπεριφορά και φωτοκαταλυτικές ιδιότητες των υλικών $\text{Zn}_{1-x}\text{Cu}_x\text{S}$ για παραγωγή υδρογόνου κάτω από ακτινοβολία ορατού φωτός αποτελεί αντικείμενο μελέτης αυτής της εργασίας. Επίσης, η περαιτέρω βελτίωση της φωτοκαταλυτικής δράσης των ετεροδομών $\text{Zn}_{1-x}\text{Cu}_x\text{S}$ με επεξεργασία με ιόντα θείου αποτελεί μια άλλη σημαντική πτυχή της παρούσας έρευνας.

Table of Contents

Chapter 1	6
1.1 Introduction	6
1.2 Nanoporous solids	6
1.3 Crystalline and amorphous porous solids	7
1.4 Mesoporous materials.....	9
1.5 Synthesis of mesoporous materials.....	10
1.6 Semiconductor photocatalysis	14
1.7 Photocatalytic water splitting into hydrogen	17
Chapter 2: Scope of the study	19
Chapter 3: Experimental techniques and details	21
3.1 Synthesis of ZnS NCs.....	21
3.2 Preparation of mesoporous ZnS NCAs	21
3.3 Preparation of mesoporous Cu-doped ZnS NCAs.....	21
3.4 Sulfur treatment of mesoporous $Zn_{1-x}Cu_xS$ frameworks	22
3.5 Physical characterization	23
3.6 Electrochemical measurements.....	24
3.7 Photocatalytic hydrogen evolution	25
Chapter 4. Physical characterization	26
4.1 Synthesis and chemical composition.....	26
4.2 Crystal structure and morphology	28
4.3 Optical absorption properties.....	33
ZnS	34
4.4 Photocatalytic study.....	34
4.5 Recycling study of $Zn_{0.95}Cu_{0.05}S'$ NCAs catalyst	39
4.6 Electrochemical properties	41
Conclusions	45
References	47

Chapter 1

1.1 Introduction

The design and development of novel nanoporous structures have attracted significant attention in the past few years due to their potential application in wide areas of science and technology, including light energy conversion, environmentally friendly photocatalysis, sensors, tissue engineering, DNA sequencing, drug delivery and photonic devices [1]. Porous materials, in general, have a key function in applications where molecular recognition is needed, such as size-selective catalysis, absorption, chemical sensing and gas separation. Among porous solids, the mesoporous metal chalcogenides are particularly important because they possess tunable electronic and optical properties and exhibit large internal surface area with remarkable redox activity [2]. With these attributes, they show great perspectives for applications in light energy conversion, photocatalysis, and Li-ion batteries [3].

Metal chalcogenides can be categorized as semiconductors due to the energy gap difference between the conduction and valence band. In 1972, Fujishima and Honda discovered the hydrogen generation by illuminating TiO_2 electrode in a photoelectrochemical cell (PEC) [4]. Briefly, semiconductor photocatalysis involves a photochemical catalytic reaction on the surface of a semiconductor material [5]. When a semiconductor absorbs photons with energy greater than the bandgap (E_g), electrons are excited to the conduction band, leaving holes in the valence band. The separated electrons and holes (excitons) then migrate through the semiconductor structure to the solid/electrolyte interface, where redox reactions occur to produce fuels or chemicals. The photocatalysis can find applications in several fields such as hydrogen and oxygen generation, water treatment and fine organic synthesis [6,7,8].

1.2 Nanoporous solids

Nanoporous materials can be found in nature, biological systems and natural minerals. By definition, a porous matter is considered as a material that has voids throughout its structure. The voids may exhibit a translational repetition or may appeared in a random

order in the 3D space. Porous solids are a unique category of composite materials consisting of an inorganic or organic polymer structure penetrated by a continuous network of connected pores. The chemical behavior and reactivity of porous solids are generally affected by morphological aspects such as internal surface area, pore volume and pore size distribution. According to the definition by IUPAC, porous solids can be classified primarily based on their pore sizes to *microporous* with pore sizes less than 2 nm, *mesoporous* with pore sizes between 2 and 50 nm, and macroporous materials with pore sizes exceeding 50 nm [9]. A good analytical technique for the estimation of pore size distribution and total pore volume in nanoporous materials is the nitrogen physisorption analysis [10,11]. Indeed, pores of different sizes and geometries yield totally different shapes of sorption isotherms.

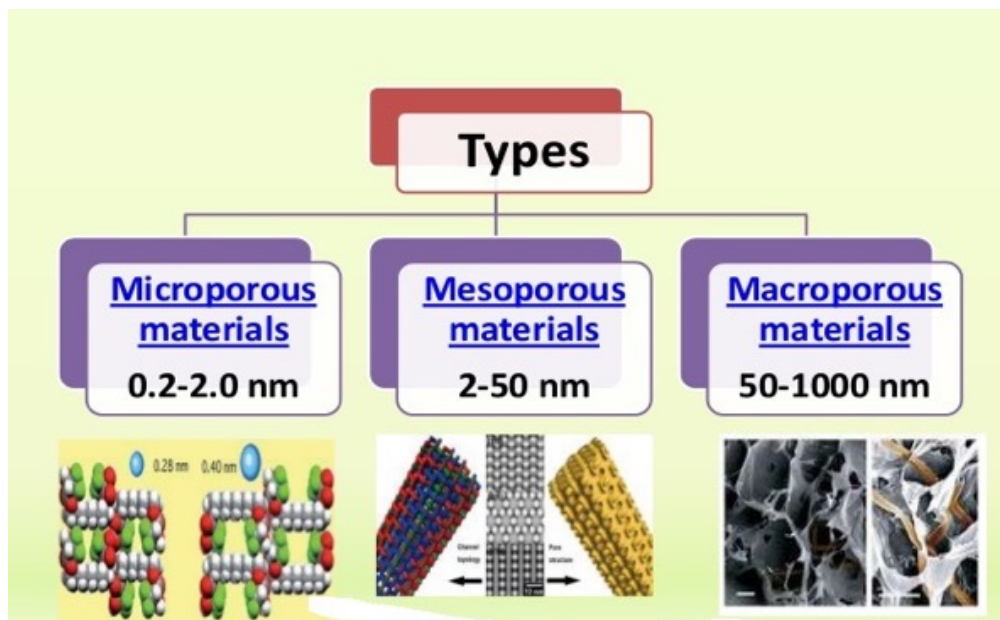


Figure 1: Categories of porous materials according the porous size.

1.3 Crystalline and amorphous porous solids

In general, porous solids based on their constructing authorities can be labeled as amorphous, crystalline and structured materials.

- *Amorphous porous solids* generally are called the materials that their framework does not comprise any particular build of atoms or molecules. Also, amorphous materials don't follow any geometry and periodic arrangement of components at the nanoscale and mesoscale level. Usually they are synthesized by sol-gel method using metal chloride or nitrate precursors [12,13,14].
- *Porous crystalline solids* considered when the atoms of the material's framework are placed in a repeated periodic arrangement. So, a long-range order occurs and, during the solidification process, the atoms form a repeated three-dimensional structure. The well-ordered structure originates from the intrinsic nature of the constituent particles to form symmetric patterns that repeat along the principal directions of three-dimensional structure in matter. The crystal structure and symmetry of the matrix plays a key role in determining many physical properties, such as electronic band structure, electronic conductivity and optical transparency.
- *Structured porous solids* consist of structural units which mimic a physical structure formed by a template. The pores in these materials also have a defined geometry and arrangement. The main representative of this class of materials are the organized mesoporous silicate materials (e.g. MCM, SBA, CMK type).

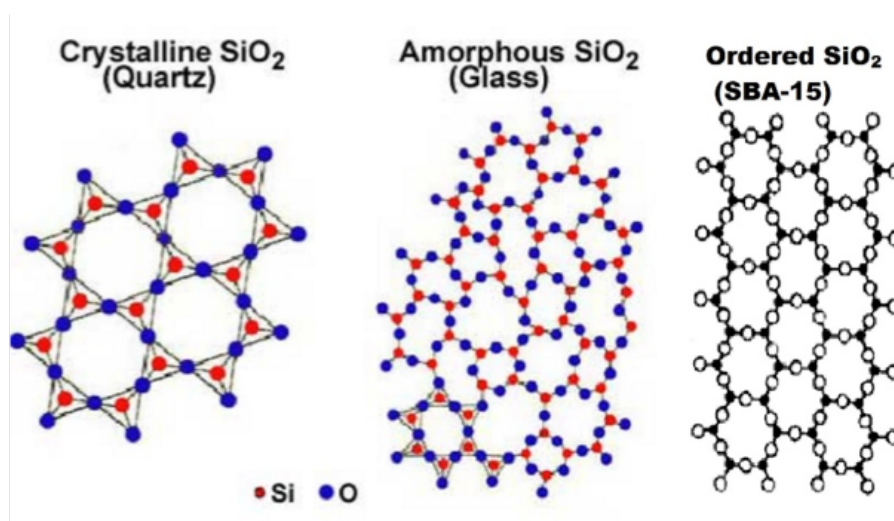


Figure 2: Crystal structure of solid materials.

1.4 Mesoporous materials

Mesoporous materials are gaining growing research interest because of their useful characteristics such as large internal surface area and pore volume, well-defined pore size distribution, controllable wall composition, and modifiable surface functionality. These materials can exhibit a highly ordered and size-controlled porous structure, which is beneficial for size-selective separation of small molecules, providing a molecular weight reduce-off enhancement. In 1992 researchers of Mobil Oil Corporation proposed the synthesis of hexagonally packed mesoporous silicate and aluminosilicate materials with uniform pores – these porous solids were termed MCM-41. The synthesis of MCM-type porous materials was achieved by means of the use of surfactant micelles as structure directing agents in a sol-gel process. Briefly, amphiphilic organic molecules can be self-assembled into cylindrical micelles in a polar solvent, which are encapsulated by inorganic species that balance the charge on the micellular surface. Thermal treatment at elevated temperatures (e.g. 500-600 °C) can then be used to decompose the organic species inside the pores, leaving behind a hexagonal arrangement of mesopores. The most known and well-studied material is the mesoporous silica MCM-41 with one-dimensional (1D) hexagonal arrangement of pores. The cubic MCM-48 exhibits a three-dimensional (3D) pore structure that is more resistant to pore clogging and allows faster diffusion of reactants inside the pore channels (Figure 3).

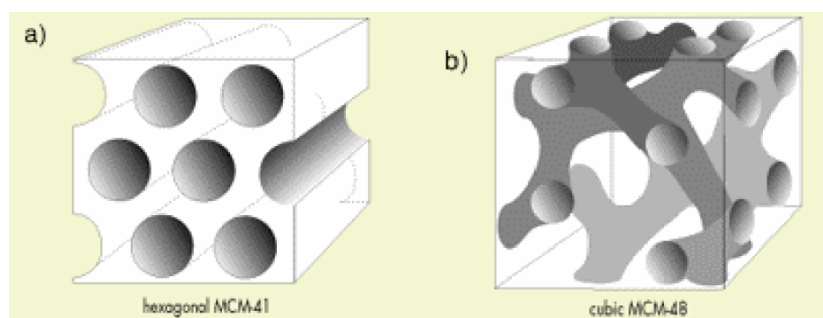


Figure 3: Mesoporous silicates were reported by Mobil Oil scientists in 1992: (a) MCM-41, which stands for Mobil Composition of Matter No. 41, shows a highly ordered hexagonal array of one-dimensional pores with a very narrow pore size distribution. The walls, however, resemble amorphous silica. (b) MCM-48 has a cubic mesostructure, i.e. arrangement of the pores.

The major challenges in research of nanoporous materials include the understanding of structure-property relations and tailor-design of nanostructures for specific applications. A significant development has been made in the control of the pore shape and sizes and active sites' activity and distribution. Catalysis by mesoporous materials at present covers a wide range of economically important processes related to the upgrading of crude oil and natural gas and the production of high quality fine chemical products [15]. All reactions and conversions are based on the acid and redox properties and shape-selective behavior of the porous structure. The most common reactions, where nanoporous acid-catalysts are used, are fluid catalytic cracking, hydrocracking, aliphatic alkylation, oligomerization, transformation of aromatics and conversion of methanol to hydrocarbons.



Figure 4: Applications of photocatalysis.

1.5 Synthesis of mesoporous materials

The inspiration for synthesizing mesoporous materials comes from nature, which has developed such structures for performing tasks swiftly and with excessive efficiency. For the creation of mesopores, self-assembled molecular aggregates or supramolecular assemblies of organic amphiphilic molecules (surfactants) are generally employed, while for creation of macroporosity, large-sized components such as colloidal crystals, emulsions or vesicles are added in the synthesis. According to these synthetic methods, desired pore

sizes can be obtained with the aid of adjusting the synthesis parameters, including the metal oxide precursors, solvent, pH of solution, temperature, and type of templates. The template synthesizing route includes soft template [16] and hard template [17] methods (Figure 5). The former structure depends on the ability of organic molecules to assemble extended nanostructures, while the inorganic lattice replicates these organic aggregates through physical or chemical interactions.

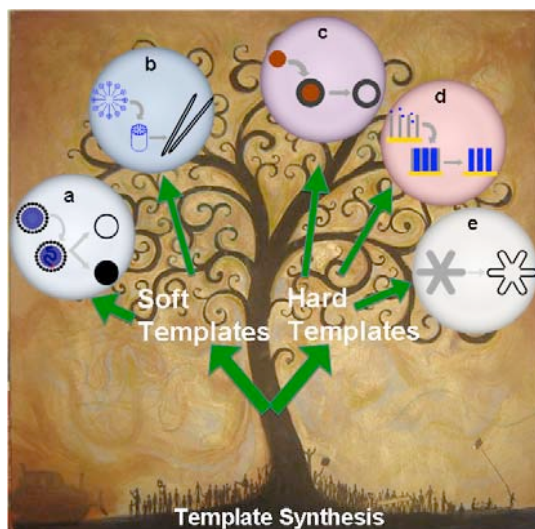


Figure 5: Illustration of the template synthesizing routes: (a) microemulsion and reversed-microemulsion synthesis, (b) non-template synthesis, (c) physical templating against existing nanostructure of particles, (d) structural replicate of nanochannel, and (e) reactive template method.

The soft template synthesis

Various chemical methods are used to prepare mesoporous materials. However, the most widespread and efficient method of synthesis is that of liquid-crystal template (LCT). In this method, well organized micelles of organic amphiphilic molecules or block copolymers (surfactants) are formed in a polar solution (e.g., water or ethanol). At the surface of micelles, the inorganic matter is then organized and polymerized forming a continuous polymeric network. This approach is general and it can be applied to the development of ordered inorganic materials with dimensions ranging from a few nanometers to a few micrometers.

The mechanism for the formation of the micelles has been extensively investigated in recent years through many studies, but yet remains unclear [18]. Among various suggestions, Beck et al. proposed a liquid-crystalline surfactant model, which seems to describe well the development of these materials [19]. According to this mechanism, a liquid crystalline phase of organic molecules is formed first, which then reacts with the inorganic species (e.g. metal oxide-hydroxide monomers or oligomers) in the solution by electrostatic forces and/or hydrogen bonding interactions (Figure 6). Next the inorganic components are cross-linked together by a chemical sol-gel process on the surface of micelles to produce organized hybrid inorganic-organic composites. Finally, the organic species within the pores are removed by high-temperature heating (400–600 °C) or ion-exchange to produce mesoporous material with open-pore structure and large internal surface area. The porous structure of these materials is defined by the micelle structure and exhibits usually cubic or hexagonal symmetry.

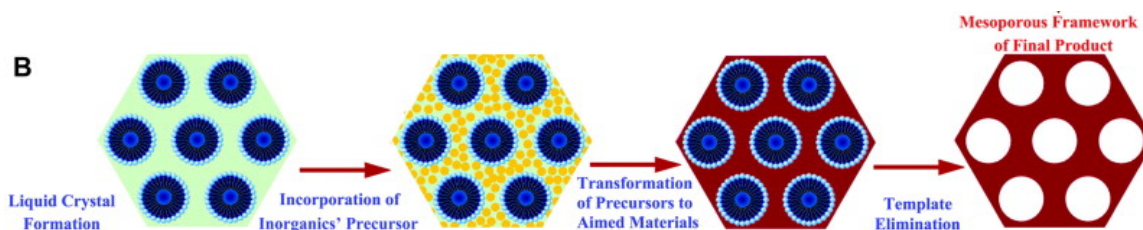


Figure 6: Schematic illustration of synthesis via liquid-crystal template (LCT) technique.

Templated assembly of colloidal nanocrystals

Polymer templating of inorganic materials has been also regarded as an effective method to produce mesostructured architectures consisting of connected nanoparticles with high porosity and uniform pores [20]. This approach, although it has been initially proposed for the synthesis of ordered mesoporous frameworks of metal oxide compounds, also seems to be well-suited for assembly of colloidal nanocrystals (NCs) into 3D open-pore structures. Briefly, this method manipulates the NCs as functional building blocks and relies on the arrangement and connection of these nanoscopic units into porous morphologies with the aid of block copolymer (BCP) structure-directing agents. The co-assembly of NCs with BCP template likely occurs by supramolecular chemistry via a solvent evaporation-induced

aggregation process, in which slow evaporation of solvent drives the aggregation of hybrid BCP–NC composites. Finally, the organic components from the hybrid mesostructure can be removed by calcination or ion-exchange to give NC-linked mesoporous frameworks with accessible pore channels. Recently, our group demonstrated that this method can be used for the synthesis of high-surface area mesoporous networks of connected BiFeO₃ NCs; in particular, this approach uses BiFeO₃ NCs coated with 3-aminopropanoic acid (3-APA) as starting materials and utilizes poly(ethylene oxide)-*block*-poly-(propylene oxide)-*block*-poly(ethylene oxide) BCPs to template the aggregating self-assembly of these nanoscopic elements (Figure 7) [21,22,23].

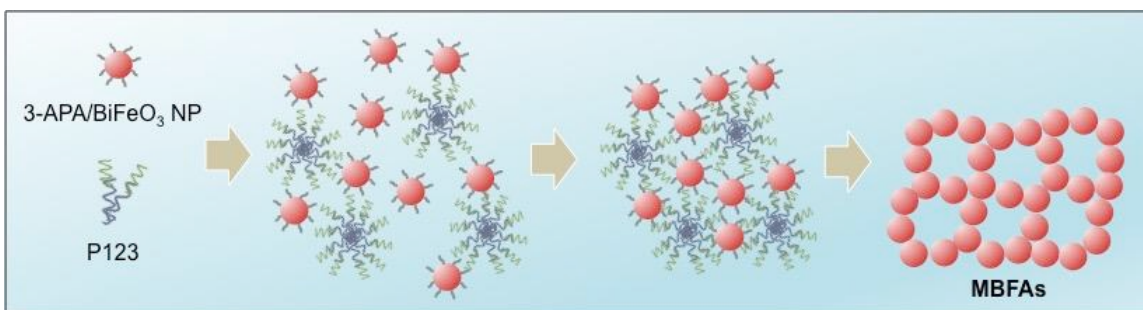


Figure 7: Schematic illustration showing possible reaction route for the formation of mesoporous BiFeO₃ nanoparticle assemblies (MBFAs).

Colloidal crystal templating

Colloidal crystal templating is generally used to fabricate 3D macroporous networks with pore diameters of a few hundred nanometers, although some examples for the synthesis of mesoporous structures have been reported. The concept of colloidal crystal templating is similar to the nanocasting method, that is, a precursor solution fills the interstitial spaces in close-packed arrays of colloidal crystals. Then the inorganic precursors are solidificated during thermal heating between the crystals, followed by removal of the template to give an inverse replica structure. The combination of soft-templating and colloidal crystal templating methods provides an effective way for the synthesis of ordered porous structures with both interconnected mesopores and macropores. The colloids typically have particle sizes of at least a few tens of nanometers which can be self-aggregated into 3D close-packed structures. The obtained arrays allow

infiltration of the inorganic precursor and surfactant solution in the voids between the colloidal spheres. Finally, after solidification of the inorganic framework and removal of the surfactants and colloidal templates, a 3D ordered meso-/macroporous structure can be obtained (Figure 8) [1].

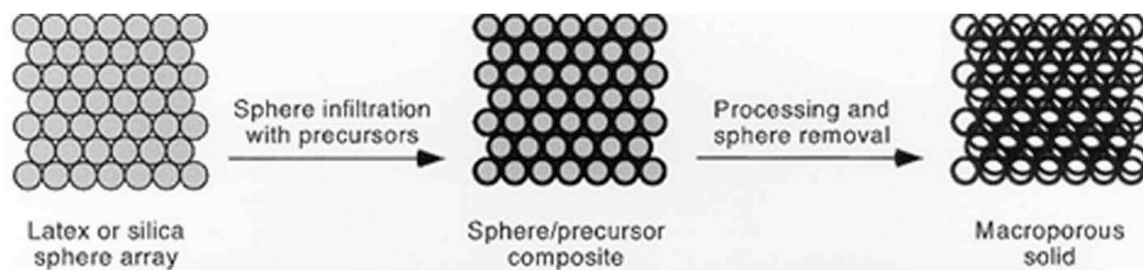


Figure 8: Synthetic process of the colloid crystal templating method.

1.6 Semiconductor photocatalysis

Over the last decades the scientific interest in applications of semiconductor photocatalysis has grown significantly. Semiconductor photocatalysis has been applied to a variety of technological challenges, including fine chemical synthesis, light energy conversion, solar fuel production and environmental remediation. Semiconductors, like TiO_2 , ZnO , Fe_2O_3 , CdS , and ZnS , can act as sensitizers for light-initiated redox reactions due to their appropriate electronic band structure that absorbs light and creates electrons in the conduction band (CB) and holes in the valence band (VB). The electronic structure of semiconductors is characterized by the presence of a bandgap (E_g), which is in fact an energy interval between the VB and CB edges. In the context of electron transfer between semiconductors and aqueous redox species, it is critical to perceive the highest occupied and the lowest unoccupied electronic stages in the semiconductor due to the fact that those energy levels are involved in the charge transfer. The Fermi level (E_F) represents the chemical potential of electrons in a semiconductor and for an intrinsic semiconductor, the E_F corresponds to the energy halfway between the CB and VB edges.

When photons of energy equal to or higher than the E_g reaches the semiconductor surface, an electron is promoted from the VB into the CB leaving a hole behind. Excited

conduction-band electrons can drop back into the valence band emitting the absorbed energy as photons or heat. Moreover, excited electrons can get trapped in metastable surface states or react with electron acceptors adsorbed on the semiconductor surface. In the absence of suitable electron and hole scavengers, the absorbed energy is dissipated within a few nanoseconds by recombination. However, electron-hole recombination can be largely suppressed and subsequent redox reactions may occur when a suitable scavenger or surface defect state is available to trap the excitons. The conduction-band electrons are good reductants (+0.5 to -1.5 V vs NHE), while the valence-band holes are good oxidants (+1.0 to +3.5 V vs NHE) (Figure 9) [24].

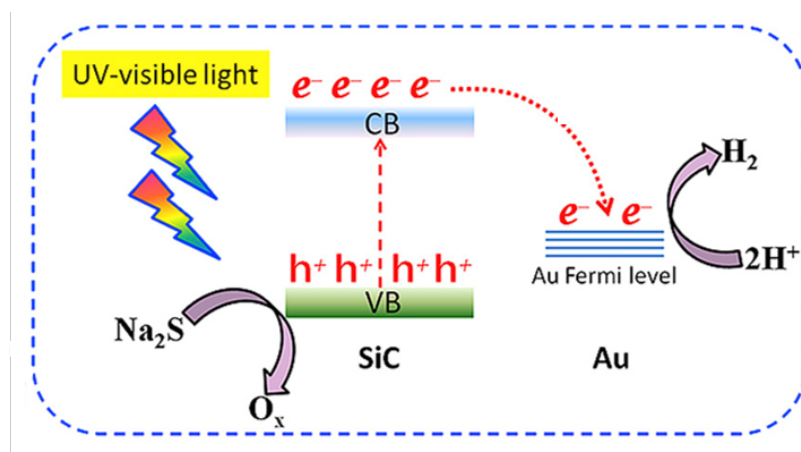


Figure 9: Schematic diagram of semiconductor photocatalysis.

Instead of the use of a single-component semiconductor, combining a semiconductor with metals (co-catalyst) or other semiconductors would lead to the formation of a heterojunction structure. These heterojunctions had been observed to enhance the light-energy conversion performance of a variety of devices, such as photocatalysts, solar cells, photoluminescent and electro-chromic devices, in a way as described below.

A co-catalyst is a compound added to the photocatalyst semiconductors to improve their charge separation and catalytic properties. In photocatalytic water splitting, for example, the co-catalysts can be used to enhance either the water oxidation or reduction reactions. The co-catalysts for water reduction reaction are usually small metal nanoparticles, which form a Schottky junction with the semiconductor surface, enhancing charge carrier

separation and, thus, photocatalytic efficiency. In principle, the contact between the metal and the semiconductor creates an internal electric field that separates the photoexcited electrons and holes, as demonstrated in Figure 9. If the work function of the metal lies below the CB edge of the semiconductor, excited electrons can inject from the semiconductor's CB to the metal nanoparticles, where they can react with protons to produce hydrogen. In addition, noble metal nanoparticles, such as Au and Pt, may provide active sites for hydrogen evolution due to their quite low over-potential for water reduction.

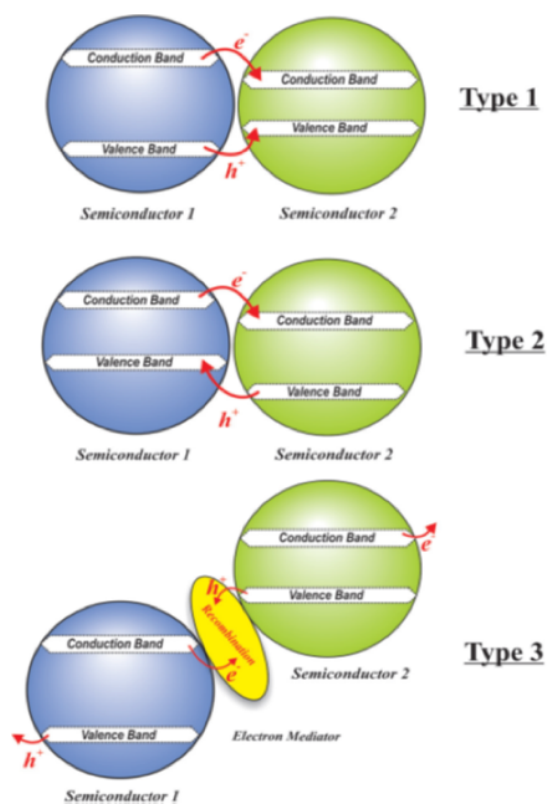


Figure 10: Various types of heterojunctions.

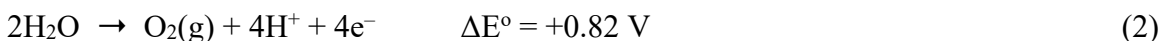
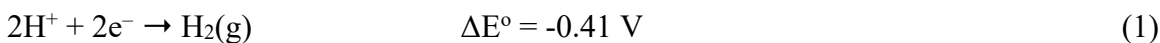
On the other hand, the utilization of nanocomposites as photocatalysts is another efficient and potential approach to enhance the photocatalytic performance. In this type of composite materials, if the second semiconducting component has a suitable band-edge position to accept electrons or holes, then excited charges can migrate from one semiconductor to another. Furthermore, this approach can enhance the overall catalytic efficiency due to the fact that the reduction and oxidation reactions may take place in

different components. All heterojunctions can be classified into three types primarily based on their conduction and valance band positions, as illustrated in Figure 10.

- ❖ Type I heterojunction, each excited electron and hole transfer from semiconductor 1 to semiconductor 2 due to their band edge positions. Usually this type of heterojunction does not enhance the photocatalyst's efficiency due to the fact of the accumulation of both charge carriers on one semiconductor.
- ❖ Type II heterojunction, both the conduction and valence bands of semiconductor 2 are below than those of the semiconductor 1. As a result, excited electrons can inject from semiconductor 1 to semiconductor 2, even though generated holes migrate vice versa. If both semiconductors have enough intimate contact, an efficient charge separation will occur during the course of light irradiation. Consequently, electron-hole recombination is reduced and so charge carriers have a longer lifetime, leading to higher photocatalytic activity.
- ❖ Type III heterojunction consists of semiconductors in which both the valence and conduction band edge positions of one semiconductor are lower than those of the other semiconductor. This type of heterojunction can be applied in a Z-scheme photocatalytic system with a suitable electron-hole mediator that attaches the two semiconductors [25].

1.7 Photocatalytic water splitting into hydrogen

Hydrogen production via photocatalytic water splitting using sunlight has an enormous potential to solve the worldwide energy and environmental crisis. However, the efficiency of solar-water-splitting systems is still too low for practical applications, which requires further enhancement via different strategies such as doping, construction of heterojunctions, morphology control, and optimization of the crystal structure. The overall water reduction reaction is composed of two half-reactions, the hydrogen evolution reaction (HER, Eq. 1) and the oxygen evolution reaction (OER, Eq 2).



Photocatalytic water splitting involves complicated photoelectrochemical reactions (Figure 11). In particular, during this photocatalytic process, electrons within the VB of the semiconductor photocatalyst are excited by the incident light to the CB, leaving behind holes in the VB (Figure 11, step I). Then, the photogenerated electrons and holes migrate to the surface-active sites, where the HER and OER takes place, respectively (Figure 11, step II). At the same time, electron–hole pairs tend to recombine (Figure 11, step III), which is an unfavorable process that lowers the overall catalytic efficiency [26]. In general, a highly active photocatalyst is expected to have proper bandgap and energy band positions to ensure absorption of sufficient solar-light and realize overall solar water splitting; its CB minimum must be higher in energy than the redox potential of H^+/H_2 couple (-0.41 V vs. NHE, pH 7), while the top of VB level must exceed the oxidation potential of H_2O to O_2 (0.82 V vs. NHE, pH 7) [27]. Moreover, the photocatalyst should have a high conductivity for charge carriers and exhibits fast surface reaction kinetics.

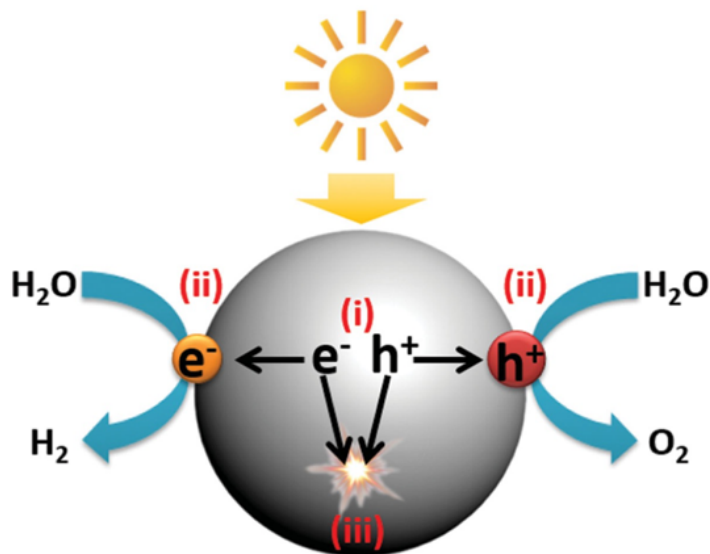


Figure 11: Schematic illustration of different steps during the solar-water splitting process: (i) generation of electron–hole pairs by light irradiation, (ii) migration of electrons and holes to the surface-active sites for HER and OER and (iii) recombination of electron-hole pairs.

Chapter 2: Scope of the study

This master thesis aims on synthesis of new 3D mesoporous networks consisting of interconnected Cu-doped ZnS ($Zn_{1-x}Cu_xS$; $x = 0.02, 0.05, 0.10$) nanocrystals and investigation of their photocatalytic performance for hydrogen evolution under visible light irradiation. The $Zn_{1-x}Cu_xS$ heterostructures were prepared by a facile wet chemical method, which includes cooperative self-assembly of colloidal ZnS nanocrystals and block copolymer aggregates, followed by chemical transformation of the ZnS components via a partial cation-exchange treatment to replace Zn^{2+} with Cu^+ . The crystal structure, morphology and chemical composition of the prepared materials were characterized by powder X-ray diffraction (XRD), transmission electron microscopy (TEM), energy-dispersive X-ray spectroscopy (EDS) and N_2 physisorption measurements. According to these results, the obtained $Zn_{1-x}Cu_xS$ nanocrystal networks contain various loadings of Cu (ranging from 2 to 10 mol%) and exhibit a 3D nanoporous network with large internal BET surface area (up to $313 \text{ m}^2/\text{g}$) and narrow pore-size distribution (ca. 3.5–5.5 nm in diameter). Also, the pore walls of these materials consist of connected zinc-blende-structured ZnS nanoparticles and exhibit high crystallinity. The electronic properties and photochemical behavior of the $Zn_{1-x}Cu_xS$ assemblies were investigated by UV-vis/NIR optical absorption and electrochemical impedance spectroscopy.

The combination of a semiconducting framework with large internal surface area makes these materials highly promising for application in photocatalytic water splitting for hydrogen production. The ZnS is an II-VI semiconductor with a wide band gap; the cubic ZnS has a band gap of about 3.54 eV. Semiconductor photocatalysts with large band gap (above 3.2 eV in energy), however, are mostly active only under UV light, which accounts only 4% of the total sunlight radiation. Therefore, photocatalysts for viable solar fuel production need to operate under visible light irradiation. That's why we study the effect of different amounts of Cu incorporated into the crystal structure of ZnS in order to tune the band gap of $Zn_{1-x}Cu_xS$ composites and enhance their visible light absorption. A great aspect of this study is the further improvement of the photocatalytic activity of Cu-doped ZnS frameworks by sulfur treatment. The photocatalytic H_2 -production activity of the Zn_{1-x}

$x\text{Cu}_x\text{S}$ nanocrystal assemblies was evaluated by visible light irradiated ($\lambda > 420 \text{ nm}$) reduction of water.

Chapter 3: Experimental techniques and details

3.1 Synthesis of ZnS NCs

The synthesis of ZnS nanocrystals (NCs) was achieved using zinc chloride (ZnCl_2) and sodium sulfide ($\text{Na}_2\text{S}\cdot 9\text{H}_2\text{O}$) as reagents and 3-mercaptopropionic acid (3-MPA) as capping agent. In a typical synthesis, 10 mmol of ZnCl_2 , 10 mmol of Na_2S and 10 mmol of 3-MPA were added under stirring to 50 mL of water, and the solution pH was adjusted to 10 using NaOH solution. After stirring for about 1 h, the MPA-capped ZnS NCs were isolated by precipitation with the addition of 2-propanol and dried at 60 °C for 24 h.

3.2 Preparation of mesoporous ZnS NCAs

In typical experiment, 250 mg of block copolymer Brij-58 ($\text{HO}(\text{CH}_2\text{CH}_2\text{O})_{20}\text{C}_{16}\text{H}_{33}$, $M_n \sim 1124$) was dissolved in 2.5 mL of water inside a 50 ml glass beaker. To this solution, MPA-capped ZnS NCs dispersed in 2.5 mL water (~ 1.7 mmol) was added and the resultant dispersion was left stirring for 1 h at room temperature. Then, 2 mL of 1 wt % H_2O_2 in water was added dropwise and the mixture was kept under stirring until gelation was observed (typically within ~ 1 h). The obtained mixture was placed in an oven for 3 days at 40 °C to evaporate the solvent under static conditions. Finally, the template was removed by soaking the gel product once in 20 mL of ethanol for 2 h and three times in 20 mL of water for 15 min. The mesoporous samples were filtrated under vacuum, washed several times with water and ethanol, and dried at 60 °C for 12 h.

3.3 Preparation of mesoporous Cu-doped ZnS NCAs

The $\text{Zn}_{1-x}\text{Cu}_x\text{S}$ photocatalysts were synthesized via a partial cation exchange reaction of Zn(II) with Cu(I) ions (Figure 13). Briefly, 100 mg of as-prepared ZnS mesoporous material was dispersed in 20 mL of water containing different amounts of CuCl. A series of Cu-doped ZnS NC assemblies with 2, 5 and 10 mol% of Cu content (denoted as $\text{Zn}_{1-x}\text{Cu}_x\text{S}$ NCAs; $x = 0.02, 0.05, 0.1$) was obtained by varying the initial Cu(I) concentration in the reaction mixture.

3.4 Sulfur treatment of mesoporous $Zn_{1-x}Cu_xS$ frameworks

The sulfur treatment was realized on three different steps of the synthesis, in order to investigate how the S vacancies affects the photocatalytic properties of our $Zn_{1-x}Cu_xS$ materials. In general, defects can act as trap sites for charge carriers, leading to the recombination of photogenerated electrons and holes and, therefore, reducing the photocatalytic activity. Therefore, controlling the quantity of defect sites in the ZnS lattice is critical in the photocatalytic reaction.

- S-treatment of ZnS NCs: In a typical experiment, 1 mmol of as-prepared ZnS NCs and 1 mmol of Na_2S were dispersed in 10 mL of water, and the mixture was kept under stirring for 2 h at room temperature. After that, the S-treated NCs were isolated by precipitation with the addition of 2-propanol and dried at 60 °C for 24 hours. The next step was to produce mesoporous structure of 5% Cu-doped ZnS NCs (denoted as 5% Cu/ZnS_S'), following a method as described above, by using S-treated ZnS NCs as starting building blocks.
- S-treatment of ZnS NC assemblies: In a typical experiment, 1 mmol of ZnS NC assemblies was dispersed in 10 mL of water containing 1 mmol of Na_2S and the resulting mixture was stirred for 2 h at room temperature. The S-treated ZnS (ZnS') NCAs was isolated by centrifugation, washed several times with water and ethanol, and dried at 60 °C for 24 h. The next step was to dope the ZnS' mesoporous sample with Cu(I) (5 mol%) following the method as described above, giving the S-treated 5% Cu/ZnS material (denoted as 5% Cu/ZnS').
- S-treatment of Cu-doped ZnS NC assemblies: In a typical experiment, 0.25 mmol of $Zn_{0.95}Cu_{0.05}S$ photocatalyst was added to 0.25 mmol of Na_2S in 10 mL of water, and the resulting mixture was kept under constant stirring for 2 h. The S-treated mesoporous sample (denoted as $Zn_{0.95}Cu_{0.05}S'$ NCAs) was isolated by centrifugation, washed several times with water and ethanol, and dried at 60 °C for 24 h.

3.5 Physical characterization

Nitrogen adsorption-desorption isotherms were obtained at -196 °C using a Quantachrome NOVA 3200e analyzer. Before analysis, all the samples were outgassed at 80 °C for 12 h under vacuum ($<10^{-5}$ Torr). The specific surface areas were calculated by applying the Brunauer-Emmett-Teller (BET) method [28] to the adsorption data and the pore volumes were calculated from the amount of adsorbed N_2 at the relative pressure (P/P_0) of 0.98. The pore size distributions were derived from the adsorption isotherms using the non-local density functional theory (NLDFT) method [29].

Elemental microprobe analysis was performed on a JEOL JSM-6390LV scanning electron microscope (SEM) equipped with an INCA PentaFETx3 energy-dispersive X-ray spectroscopy (EDS) detector (Oxford Instruments, UK). EDS spectra were collected for different locations of sample (at least four) using an accelerating voltage of 20 kV and a 60-s accumulation time.

Powder X-ray diffraction (XRD) patterns were recorded on a PANalytical X'Pert Pro X-ray diffractometer operated at 45 kV and 40 mA using $Cu\ K\alpha$ radiation ($\lambda = 1.5418$ Å).

X-ray photoelectron spectroscopy (XPS) measurements were carried out using a non-monochromatic AlK_{α} line at 1486.6 eV (12 kV with 20 mA anode current) and a Leybold LH EA11 electron energy analyzer operated at a constant pass energy of 100 eV and pressure $2 \cdot 10^{-8}$ mbar. The catalyst powder was pressed on a thin Pb sheet and the analyzed area was a 1.5×5 mm² rectangle, placed near the center of the powder-covered area on each specimen surface. In all XPS spectra, the binding energy of the predominant aliphatic contribution to the C 1s peak at 284.8 eV was used as a charge reference [30].

Transmission electron microscopy (TEM) images were obtained on a JEOL JEM-2100 electron microscope operated at 200 kV. Samples were prepared by drying an ethanolic dispersion of particles on a holey carbon-coated Cu grid.

UV-vis/near-IR diffuse reflectance spectra were recorded on a Perkin Elmer Lambda 950 optical spectrophotometer. $BaSO_4$ powder was used as a standard (100% reflectance). The absorption spectra were converted from diffuse reflectance data using the Kubelka-Munk function: $\alpha/S = (1-R)^2/(2R)$, where R is the measured reflectance and α , S are the

absorption and scattering coefficients, respectively [31]. The energy bandgap (E_g) of semiconductors were calculated from Tauc plots, that is, $(\alpha h\nu)^2$ as a function of energy ($h\nu$) plots [32].

Photoluminescence (PL) spectra were recorded at room temperature on a Jobin-Yvon Horiba FluoroMax-P (SPEX) spectrometer (150-W Xe lamp).

3.6 Electrochemical measurements

The analysis of experimental data of the Electrochemical impedance spectroscopy (EIS) provides information about physical and chemical processes present in the electrode/electrolyte interface such as charge-transfer resistance R_s . The R_s is related to the faradaic current flowing across the interface and the Warburg impedance which is related to the diffusion-controlled migration.

Electrochemical impedance spectroscopy (EIS) and Mott-Schottky measurements were performed in a 0.5 M Na_2SO_4 aqueous electrolyte ($\text{pH} = 7$) using a Metrohm Autolab PGSTAT 302N potentiostat. A three-electrode electrochemical cell with a Pt wire as the counter electrode and an Ag/AgCl (3M KCl) as the reference electrode was used to study the samples. Mott-Schottky plots were obtained at 1 kHz, using a 10-mV alternating current (AC) voltage amplitude. Of note, similar electrochemical results were obtained using a similar three-electrode configuration but with a stainless steel SS316 (2 mm diameter) as counter electrode. For Nyquist plots, the different current output was measured throughout a frequency range of 1 Hz to 1 MHz using a small AC perturbation of 20 mV, under open-circuit potential conditions. All the EIS experiments were conducted in the dark.

The working electrodes were fabricated as follows: 10 mg of each sample was ultrasonically mixed with 1 mL of deionized water to form a homogeneous suspension. Glass slides ($1.5 \times 2 \text{ cm}^2$) coated with fluorine-doped tin oxide (FTO, $9 \Omega \text{ sq}^{-1}$) were cleaned thoroughly by sonication in acetone and then in isopropanol for 15 min and dried at 100 °C for 10 min. Next, the FTO substrates were further treated with a UV-ozone plasma for 5 min. The samples were drop-casted into FTO substrates, which were masked with an epoxy resin to leave an exposure area of $1.0 \text{ cm} \times 1.0 \text{ cm}$, and heated for 30 min at 60 °C.

3.7 Photocatalytic hydrogen evolution

Photocatalytic experiments for hydrogen evolution were performed in an airtight Pyrex glass reactor (Figure 12). In a typical experiment, 20 mg of the catalyst was dispersed with stirring in 20 mL aqueous solution containing 0.35 M Na₂S and 0.25 M Na₂SO₃, and then the mixture was deaerated by Ar gas for at least 30 min. The reaction solution was cooled to 20 ± 2 °C using a water-cooling system and irradiated at $\lambda > 420$ nm light using a 300-W Xenon lamp (Variac Cermax). The generated H₂ was detected by taking 100 μ L of gas from the headspace of the reactor using a gastight syringe and analyzed by a Shimadzu GC-2014 gas chromatograph equipped with a thermal conductivity detector (TCD), using Ar as the carrier gas.



Figure 12: Photocatalytic setup for hydrogen evolution experiments.

The apparent quantum yield, $QY = (2 \times N_{H_2})/N_{hv}$ where N_{H_2} and N_{hv} are the numbers of evolved H₂ molecules and incident photons, respectively, were estimated by obtaining the amount of evolved hydrogen at a $\lambda = 410 \pm 10$ nm irradiation wavelength. The incident photon number was determined with a StarLite power meter equipped with a FL400A-BB-50 thermal sensor (Ophir Optronics Ltd).

Chapter 4. Physical characterization

4.1 Synthesis and chemical composition

Mesoporous assemblies of connected Cu-doped ZnS nanocrystals (denoted as $Zn_{1-x}Cu_xS$ NCAs) were prepared following a two-step chemical process. First, mesoporous ZnS NC-linked network was obtained by a polymer-templated aggregating assembly of 3-MPA-capped ZnS NCs (Figure 13).

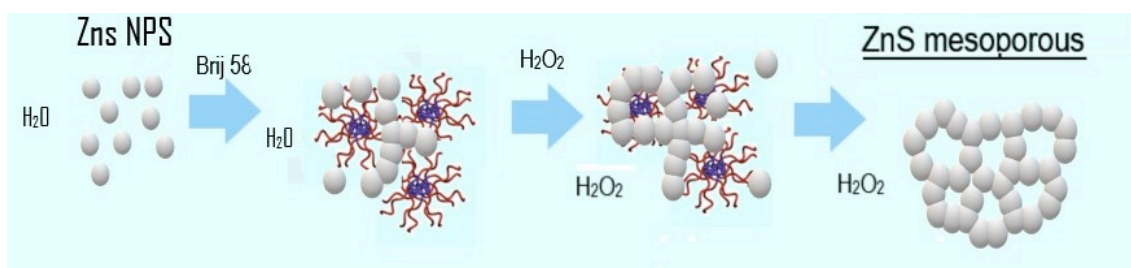
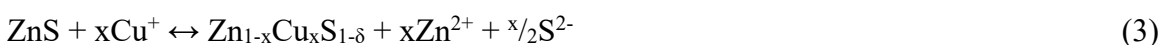


Figure 13: Schematic representation of the synthesis of ZnS NC-linked mesoporous network.

Next, Cu-doped ZnS assemblies were obtained through a chemical transformation of ZnS into $Zn_{1-x}Cu_xS$ heterostructures using a partial ion-exchange reaction of Zn^{2+} with Cu^+ ions. In the ion-exchange process, where Cu(I) replaces Zn(II) in the crystal lattice (Figure 14), the large disparity in the products solubility, i.e. K_{sp} of ZnS (4.0×10^{-24}) and Cu_2S (2.0×10^{-47}) [33], is the driving force for the spontaneously transformation of ZnS into Cu_2S , giving rise to the formation of $Zn_{1-x}Cu_xS_{1-\delta}$ (denoted as $Zn_{1-x}Cu_xS$) heterostructure (Eq. 3).



In general, the chemical transformation of ZnS into $Zn_{1-x}Cu_xS_{1-\delta}$ heterostructures involves the following steps: (i) deposition of insoluble Cu_2S on the surface of the ZnS, (ii) diffusion of Cu^+ into the ZnS lattice, (iii) interion dissolution of ZnS, (iv) diffusion of Zn^{2+} and S^{2-} ions toward the surface, and (v) interface reaction between the Cu^+ and S^{2-} ions at the inner surface of the Cu_2S particles. The growth of Cu_2S clusters within the ZnS lattice is particularly important for photocatalysis since the intimate contact between the two

semiconductors ($\text{Cu}_2\text{S}/\text{ZnS}$ junction) can suppress the charge recombination and, thus, increase the lifetime of photogenerated electron-hole pairs.

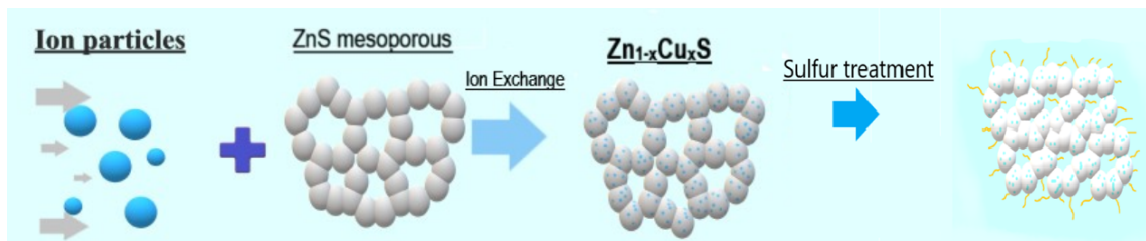


Figure 14: Schematic representation of the synthesis of mesoporous Cu-doped ZnS NC assemblies ($\text{Zn}_{1-x}\text{Cu}_x\text{S}$ NCAs) and sulfur treatment of $\text{Zn}_{1-x}\text{Cu}_x\text{S}$.

The chemical composition of the as-prepared materials was confirmed by energy dispersive X-ray spectroscopy (EDS). The EDS spectra obtained from different areas of samples showed the presence of Cu at different Zn/Cu atomic ratios, which correspond to a Cu loading from ~2 to ~10 mol% (Table 1). Figure 15 shows a typical EDS spectrum of $\text{Zn}_{0.95}\text{Cu}_{0.05}\text{S}$ NCAs sample. Of particular note, the Cu content, as determined by EDS analysis, is well consistent with the expected composition from the stoichiometry of reactions. This suggests the complete incorporation of Cu into the ZnS lattice.

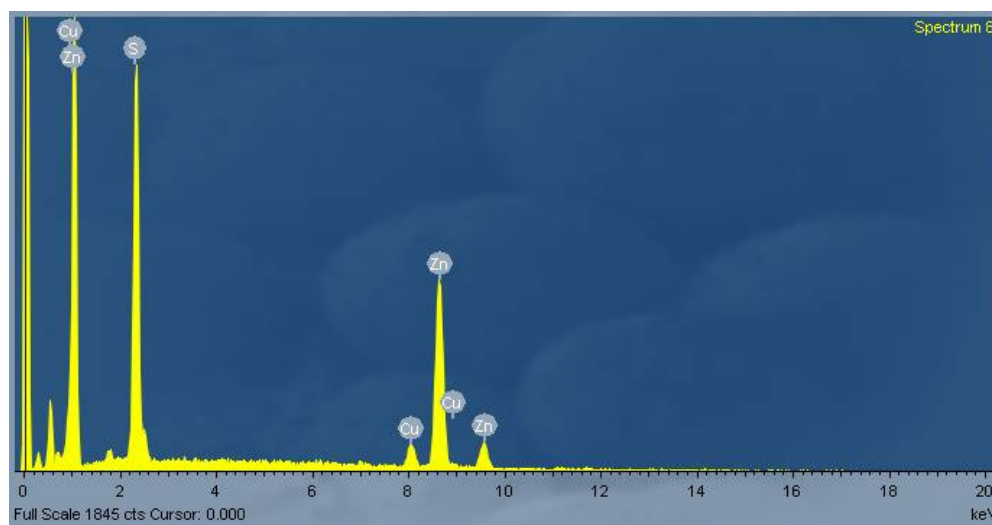


Figure 15: Typical EDS spectrum of the $\text{Zn}_{0.95}\text{Cu}_{0.05}\text{S}$ NCAs.

Table 1. EDS results and chemical formulas of the mesoporous ZnS and Zn_{1-x}Cu_xS NCAs.

Sample	Atomic ratio Zn:S:Cu	Cu loading ^a (mol%)	Chemical formula
ZnS	51.2:0:48.8	0	ZnS
2% Cu/ZnS	51.9:45.8:1.7	3.2	Zn _{0.98} Cu _{0.02} S
5% Cu/ZnS	49.7:45.2:2.7	5.1	Zn _{0.95} Cu _{0.05} S
10% Cu/ZnS	49.2:45.1:5.7	10.4	Zn _{0.90} Cu _{0.10} S
5% Cu/ZnS ^b	49.9:44.2:2.6	5.0	Zn _{0.95} Cu _{0.05} S'

^aBased on EDS analysis. ^bS-treated Zn_{0.95}Cu_{0.05}S mesoporous sample.

4.2 Crystal structure and morphology

The crystallinity and porous structure of the products was characterized by powder X-ray diffraction (XRD) and transmission electron microscopy (TEM). The XRD patterns of mesoporous ZnS, Zn_{1-x}Cu_xS and S-treated Zn_{0.95}Cu_{0.05}S' NCAs samples, in Figure 16, display three intense diffraction peaks in 2θ scattering angles from 20 to 60°, which can be assigned to the (111), (220), and (311) reflections of the ZnS zinc-blende structure with lattice parameters $a = b = c = 5.41 \text{ \AA}$ (space group F4-3m).

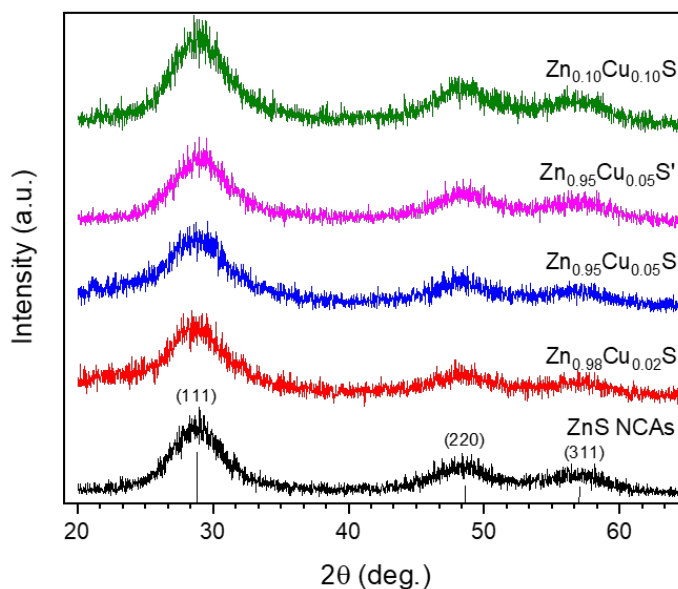


Figure 16: XRD patterns of the mesoporous ZnS and Zn_{1-x}Cu_xS NCAs.

The broadening the X-ray diffraction peaks signifies the small composition of the materials; in particular, Scherrer analysis of the peak broadening gave an average crystallite size of $\sim 2.5\text{--}3$ nm. However, XRD analysis does not provide any insightful information for the presence of Cu_xS , even in the XRD pattern of the $\text{Zn}_{0.9}\text{Cu}_{0.1}\text{S}$ NCAs sample with 10 mol% Cu. This is attributed to the small grain size and high dispersion of Cu_xS particles in the mesoporous structure.

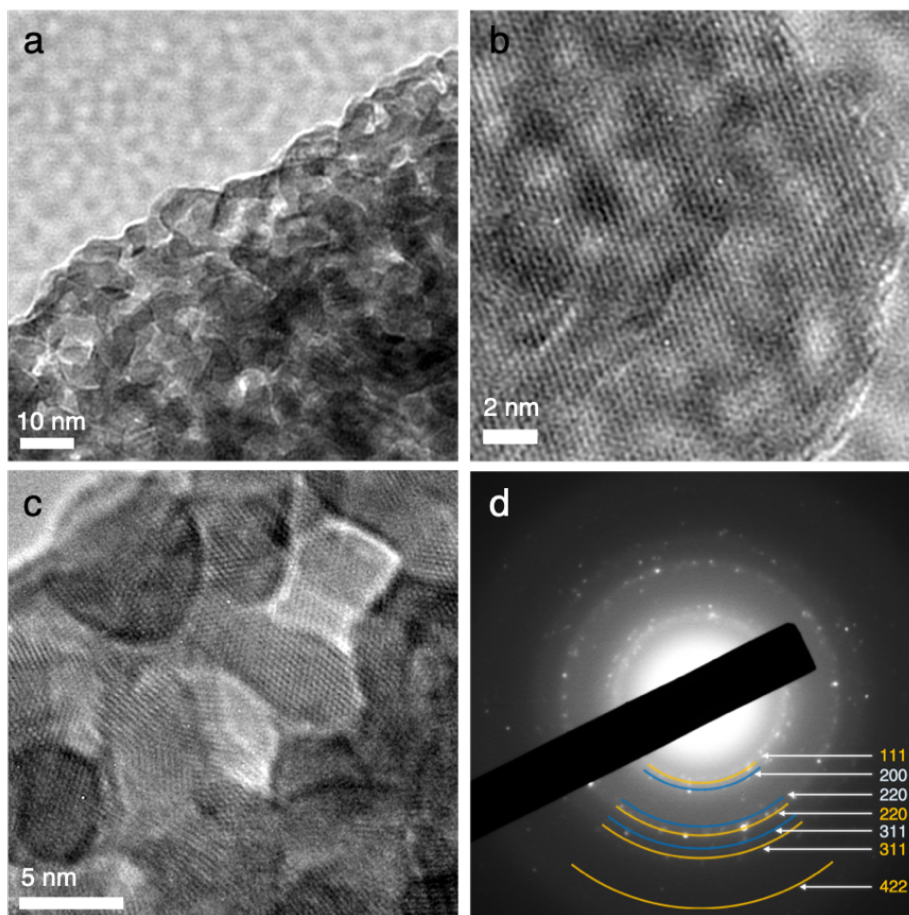


Figure 17: (a) Typical TEM image, (b, c) high-resolution TEM (HRTEM) images and (d) SAED pattern obtained from a small area of the porous structure of the $\text{Zn}_{1-x}\text{Cu}_x\text{S}$ NCAs.

Figure 17 shows typical TEM images of the $\text{Zn}_{0.95}\text{Cu}_{0.05}\text{S}$ NCAs sample, which is the most active catalyst in this study. The images reveal a porous network of connected NCs with a grain size of about 5 nm. To characterize the crystal structure of the mesoporous structure, we utilized selected-area electron diffraction (SAED). The SAED pattern shown in Figure 17d displays a series of Debye-Scherrer diffraction rings that can be assigned to

the zinc-blende structure of ZnS (marked with orange curves) and the cubic phase (space group Fm3-m) of Cu₂S (marked with blue curves). These results along with XRD data clearly indicate that the pore wall of mesoporous Zn_{1-x}Cu_xS NCAs consists of connected cubic zinc-blende ZnS and cubic chalcocite Cu₂S NCs. This supports the notion that the transformation of ZnS into Cu₂S-ZnS is topotactic in nature, that is, the crystal structure of ZnS is preserved after transformation.

The chemical state of atoms in the composite materials was studied with X-ray photoelectron spectroscopy (XPS). Figure 18 shows the high-resolution XPS spectra for the pristine and S-treated Zn_{0.95}Cu_{0.05}S NCA samples before and after catalysis. All binding energy values in the XPS spectra were calibrated according to the C 1s line at 284.6 eV. The presence of carbon mainly originated from the oil pump owing to vacuum treatment. In all materials, the Zn 2p_{3/2} photoelectron peak appears at a binding energy of ~1021.6 ±0.2 eV (Figure 18a). This position, however, does not allow a clear identification of Zn compounds, since the literature values for Zn 2p_{3/2} binding energies are similar for ZnS (1021.6 eV) and ZnO (1022.1 eV) [34,35,36,37]. For this reason, the Auger α parameter was evaluated and used to verify the presence of ZnS. According to the literature, the Zn Auger parameter, that is, the binding energy of the Zn 2p_{3/2} peak + kinetic energy of the Zn L₃M₄₅M₄₅ peak, varies from ~2010 to ~2011.3 eV for ZnS. For the Zn_{0.95}Cu_{0.05}S and Zn_{0.95}Cu_{0.05}S' NCAs the Auger parameter is measured to be ~2010.3 ±0.2 eV, which probably reflects the existence of ZnS_{1-δ} phase (Figure 18b). For the Zn_{0.95}Cu_{0.05}S' NCAs obtained after catalysis there is a significant increase in the Auger parameter value at ~2011.1 ±0.2 eV, indicating that the dominant phase is the ZnS. The Cu 2p_{3/2} core-level signal appears at a binding energy of about 932.1 ±0.2 eV, which is attributed to monovalent copper ions (Figure 18c) [38,39,40]. Generally, the 2p_{3/2} binding energy for compounds containing Cu⁺ locates at 932.6–932.8 eV [41], while that for compounds containing Cu²⁺ locates around 935 eV [42], accompanying with the characteristic Cu²⁺ shakeup satellite peaks at 938–945 eV. Taken together the SAED analysis, these results are consistent with the presence of Cu₂S species into the ZnS lattice. Meanwhile, for the S-treated Zn_{0.95}Cu_{0.05}S sample an increased concentration of divalent copper ions is presented (probably as CuS and/or Cu(OH)₂ surface species) due to the weak “shake-up”

satellite peak appeared in the higher binding energy ranges [43]. The XPS S 2p binding energies for all the samples appeared at typical positions of sulfide (S^{2-}) ions, $\sim 162 \pm 0.2$ eV. A small amount of sulfur oxides (SO_x) is however observed in the surface of S-treated $Zn_{0.95}Cu_{0.05}S$ NCAs before and after catalysis, judging from the weak feature at $\sim 169 \pm 0.2$ eV (Figure 18d).

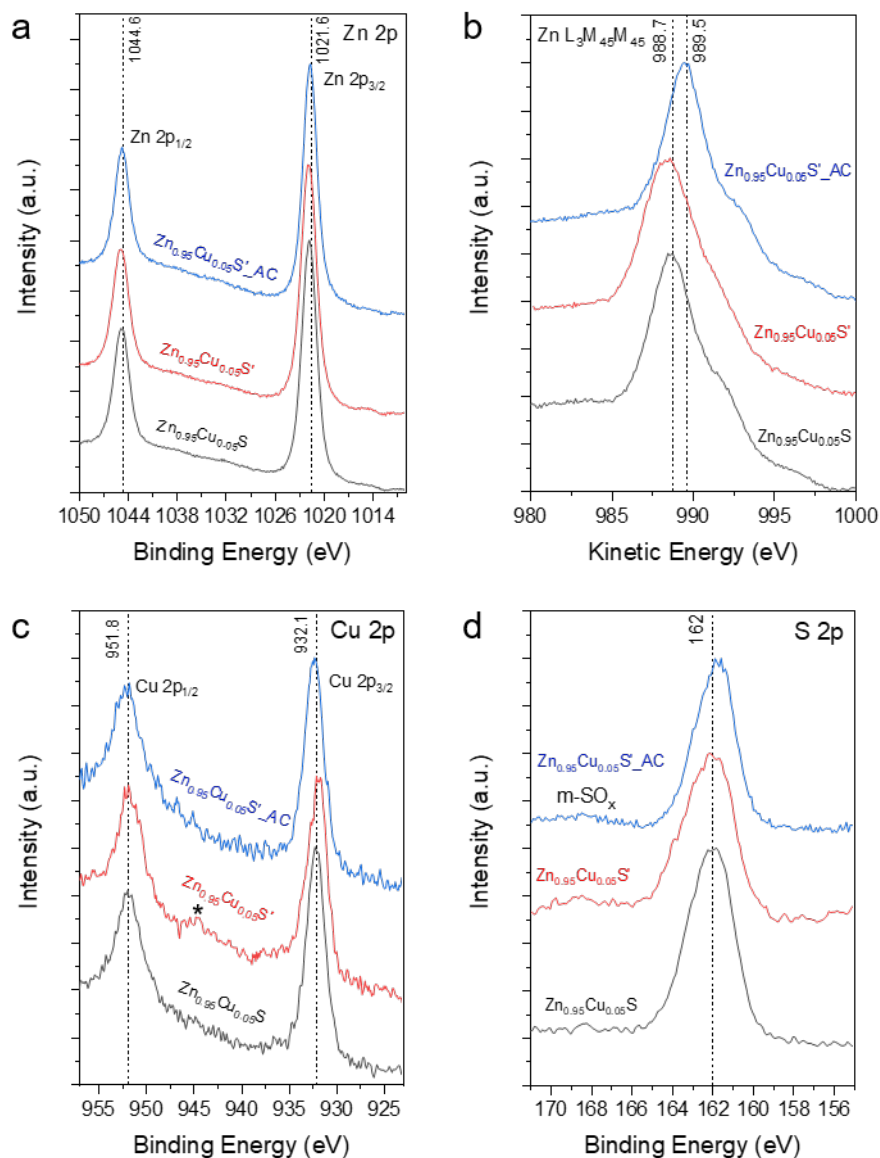


Figure 18: XPS spectra of the Zn 2p, Zn $L_3M_{45}M_{45}$ Auger, Cu 2p and S 2p core-level lines for the mesoporous $Zn_{0.95}Cu_{0.05}S$ NCAs and $Zn_{0.95}Cu_{0.05}S'$ NCAs samples before and after catalysis. In panel (c), the symbol shows the satellite peak at ~ 944.3 eV characteristic of the Cu^{2+} ions.

The porosity of the as-prepared materials was studied by nitrogen physisorption measurements at $-196\text{ }^{\circ}\text{C}$. Figure 20 shows the N_2 adsorption and desorption isotherms and the corresponding pore-size distribution plots of mesoporous ZnS and $\text{Zn}_{1-x}\text{Cu}_x\text{S}$ NCAs.

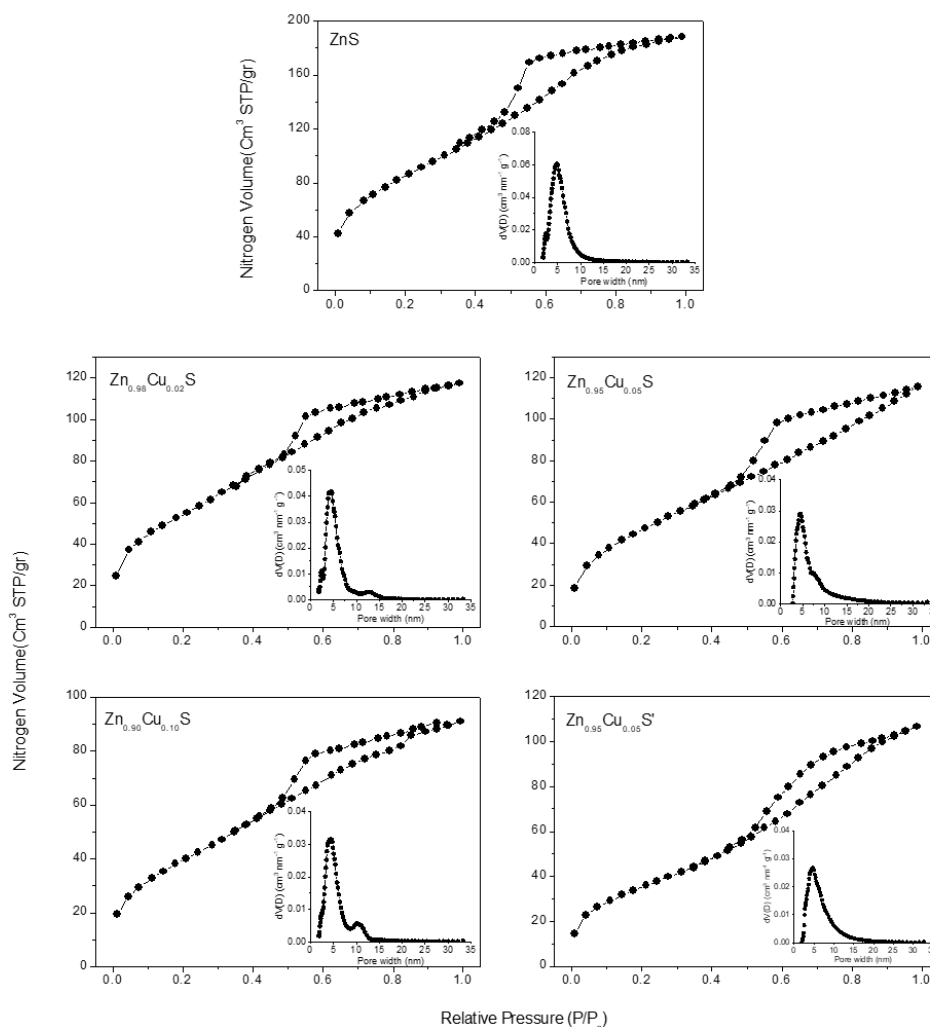


Figure 20: N_2 adsorption and desorption isotherms at $-196\text{ }^{\circ}\text{C}$ and (inset) the corresponding pore-size distribution plots for the mesoporous ZnS and, $\text{Zn}_{1-x}\text{Cu}_x\text{S}$ and $\text{Zn}_{1-x}\text{Cu}_x\text{S}'$ NCAs.

All the samples exhibited typical type-IV isotherms associated with a H_2 -type hysteresis loop (according to IUPAC classification), which are characteristic of mesoporous materials with interconnected slit-shaped pores [44]. The small but resolved adsorption step at the 0.5–0.7 relative pressure (P/P_0) range is related to the condensation of liquid nitrogen in narrow-sized mesopores. The mesoporous $\text{Zn}_{1-x}\text{Cu}_x\text{S}$ and $\text{Zn}_{1-x}\text{Cu}_x\text{S}'$ NCAs exhibited a

Brunauer-Emmett-Teller (BET) surface area of 142–235 m²/g and a total pore volume of 0.14–0.18 cm³/g, which are slightly lower than those of the pristine ZnS NCAs sample (314 m²/g, 0.28 cm³/g). The decrease in the surface area and pore volume for the Cu-loaded samples is presumably due to a partial cleavage of the ZnS NC-linked network during the ion-exchange process. The pore size in these materials was determined from the adsorption branch of isotherms using the non-local density functional theory (NLDFT) model (assuming slit-like pores). The results for ZnS and Zn_{1-x}Cu_xS NCAs reveal a quite narrow pore size distribution with an average size of ~3.5–5.5 nm (Figure 20, insets). All the textural parameters for the pristine and Cu-loaded ZnS NCAs samples are given in Table 2.

Table 2. Textural parameters of mesoporous ZnS, Zn_{1-x}Cu_xS and Zn_{1-x}Cu_xS' NCAs.

Sample	Surface area (m ² g ⁻¹)	Pore volume (cm ³ g ⁻¹)	Pore diameter (nm)
ZnS	314	0.28	4.8
Zn _{0.98} Cu _{0.02} S	235	0.18	4.5
Zn _{0.95} Cu _{0.05} S	205	0.17	4.4
Zn _{0.90} Cu _{0.10} S	150	0.14	4.4
Zn _{0.95} Cu _{0.05} S' ^a	142	0.15	4.6

^aS-treated Zn_{0.95}Cu_{0.05}S NCAs sample.

4.3 Optical absorption properties

The electronic structure of the as-prepared materials was investigated with diffuse reflectance ultraviolet-visible/near-IR (UV-vis/NIR) spectroscopy. The mesoporous ZnS and Zn_{1-x}Cu_xS NCAs show an optical absorption onset at ~330–520 nm, corresponding to their interband VB-to-CB electron transitions (Figure 21). The energy band gap is calculated to be 3.88 eV for pristine ZnS NCAs and in the range of 3.09–3.75 eV for Zn_{1-x}Cu_xS NCAs (Table 3), according to the Tauc method for a direct gap semiconductor. The large hypsochromic (blue) shift in the energy gap of ZnS NCAs relative to the bandgap of bulk ZnS (~3.7 eV) [45] is attributed to quantum size confinement in ZnS NCs due to their very small size (~5 nm according to TEM observation). The decrease in energy gap with

increasing Cu loading is related to the strong electron interactions between the electronic states in ZnS and Cu₂S NCs. This indicates that Cu₂S species were incorporated into the ZnS structure.

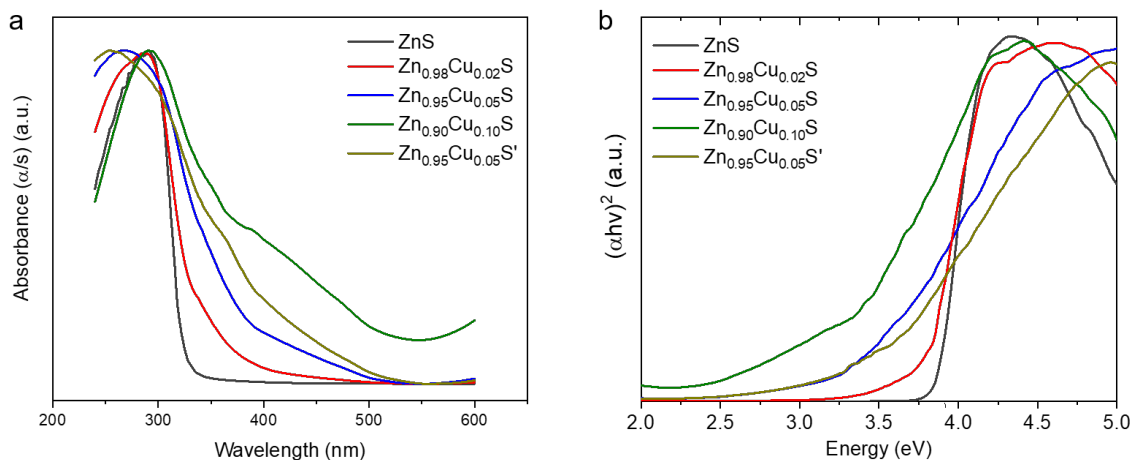


Figure 210: UV-vis/NIR diffuse reflectance spectra for mesoporous ZnS and Zn_{1-x}Cu_xS NCAs. The optical absorption spectrum of the S-treated Zn_{0.95}Cu_{0.05}S (5% Cu/ZnS) sample is also given.

Table 3. Energy band gap values for mesoporous ZnS, Zn_{1-x}Cu_xS and Zn_{0.95}Cu_{0.05}S' NCAs.

Sample	Energy band gap (eV)
ZnS	3.88
Zn _{0.98} Cu _{0.02} S	3.75
Zn _{0.95} Cu _{0.05} S	3.32
Zn _{0.90} Cu _{0.10} S	3.09
Zn _{0.95} Cu _{0.05} S'	3.36

4.4 Photocatalytic study

The photocatalytic activity of the as-prepared materials was evaluated by visible light irradiated ($\lambda > 420$ nm) reduction of water. All the photocatalytic hydrogen evolution experiments were carried out in a Pyrex glass reactor using the Na₂SO₃-Na₂S aqueous solution as sacrificial reagents. As shown in Figure 22 the mesoporous ZnS NCAs catalyst

shows a relatively low activity toward water reduction, which corresponds to a H_2 generation rate of $4.1 \mu\text{mol h}^{-1}$ mainly due to the limited visible-light absorption (it has an energy gap (E_g) of $\sim 3.9 \text{ eV}$). In contrast, Cu-loaded ZnS samples showed a considerable increase in H_2 production, indicating that the incorporated Cu_2S species into the ZnS lattice have a prominent impact on the photocatalytic performance. The catalytic activity of $\text{Zn}_{1-x}\text{Cu}_x\text{S}$ NCAs increases with increasing the Cu content and attains a maximum at 5 mol%, giving a H_2 evolution rate of $17.3 \mu\text{mol h}^{-1}$, which is about 4.2 times higher than that of single-component ZnS sample. However, further increase in Cu loading leads to a marked reduction of the photoactivity, as inferred by the lower H_2 evolution rate of the Cu/ZnS catalyst with 10 mol% Cu content ($9.7 \mu\text{mol h}^{-1}$). This is probably related to the excessive amount of Cu_2S clusters that may act as electron-hole recombination centers, decreasing the charge carrier lifetime.

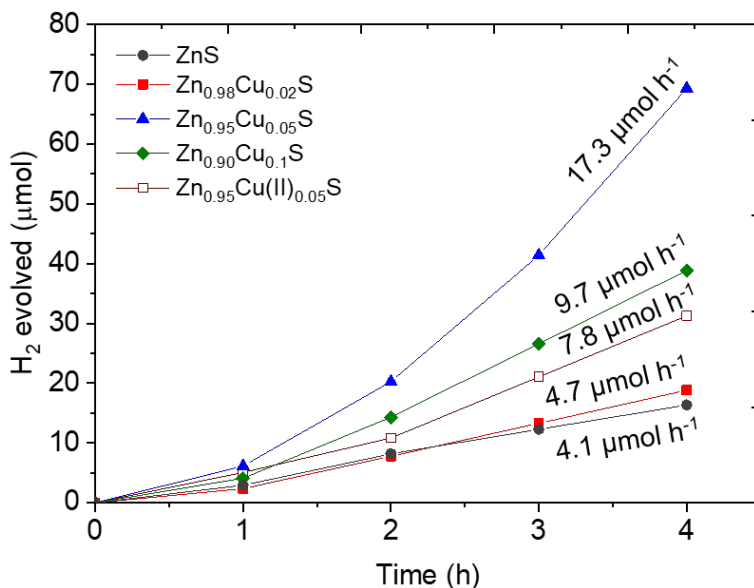


Figure 11: Time courses for photocatalytic H_2 production for mesoporous ZnS and $\text{Zn}_{1-x}\text{Cu}_x\text{S}$ NCAs. The H_2 evolution versus time for the $\text{Zn}_{0.95}\text{Cu(II)}_{0.05}\text{S}$ NCAs catalyst is also given. The H_2 evolution rates were averaged over 3 h of irradiation. All photocatalytic experiments were performed by suspending 20 mg of catalyst in 20 mL of water containing 0.25 M Na_2SO_3 and 0.35 M Na_2S , under $\lambda \geq 420 \text{ nm}$ light irradiation.

Next, we proceeded to optimize the reaction conditions by varying the catalyst concentration and the type of sacrificial agent. Figure 23 shows the H₂ evolution for different concentrations of Zn_{0.95}Cu_{0.05}S NCAs. It can be seen that the H₂ evolution rate increased with increasing catalyst addition until reaching a maximum at 1 g L⁻¹. The H₂ production increase with the catalyst concentration can be interpreted as a result of increased light absorption by the catalyst nanoparticles. However, at excess concentration of catalyst (>1.5 g L⁻¹), a saturation level is reached due to the light scattering by the colloidal particles, giving a slightly lower generation rate of hydrogen. In the following, we proceeded to investigate the effect of sacrificial electron donor on the photocatalytic H₂ production performance of Zn_{1-x}Cu_xS NCAs. Figure 24 presents comparative photocatalytic H₂ evolution results for Zn_{0.95}Cu_{0.05}S NCAs catalyst in the presence of Na₂S/Na₂SO₃ pairs, methanol, and ethanol in neutral and alkaline (5 M NaOH) solution as hole scavengers. All photocatalytic reactions were performed under visible-light irradiation ($\lambda > 420$ nm) using a fixed catalyst concentration (1 g L⁻¹). Among them, S²⁻/SO₃²⁻ pairs were found to be the most efficient sacrificial agent, resulting in a significant improvement in H₂ evolution rate ($\sim 665 \mu\text{mol h}^{-1} \text{g}_{\text{cat}}^{-1}$ in the initial 3 h).

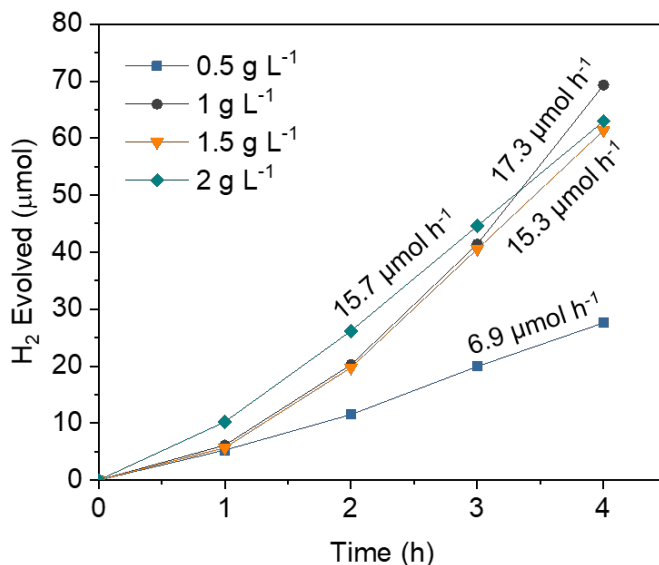


Figure 23: Time courses for photocatalytic H₂ production for different loadings of the Zn_{0.95}Cu_{0.05}S NCAs catalyst. The photocatalytic reactions were performed by suspending the catalyst in 20 mL of water containing 0.25 M Na₂SO₃ and 0.35 M Na₂S, under $\lambda \geq 420$ nm light irradiation.

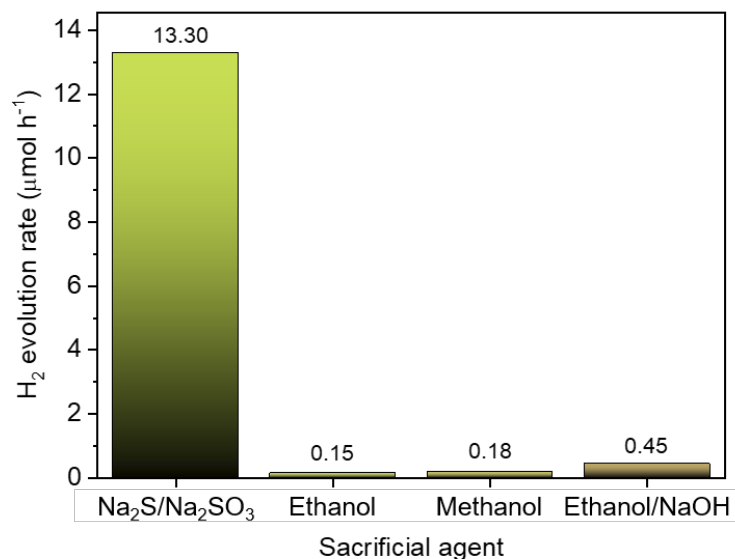


Figure 24: Photocatalytic H₂ evolution rates for Zn_{0.95}Cu_{0.05}S NCAs catalyst using different sacrificial electron donors. The photocatalytic reactions were performed by suspending 20 mg of catalyst in 20 mL of water containing the sacrificial agent, under $\lambda \geq 420$ nm light irradiation.

The incorporation of Cu⁺ ions into the ZnS lattice can induce the formation of defect sites according to the Eq. (1); in which replacement of Zn(II) by Cu(I) causes the production of sulfur vacancies in composite structure for charge balance. Such S-related defects could induce the formation of mid-gap electronic states (deep or shallow trap states), which may act as recombination centers for the photogenerated electron-hole pairs, reducing the photocatalytic activity. To rule out this possibility, we post-treated the Zn_{0.95}Cu_{0.05}S catalyst with S²⁻ solution in order to replace missing sulfur atoms in the composite structure. In particular, the sulfur treatment procedure was performed at different steps of synthesis: (i) S-treatment of starting material ZnS and then Zn_{0.95}Cu_{0.05}S synthesis from treated ZnS NCs (denoted as 5% Cu/ZnS_S'), (ii) S-treatment of mesoporous assemblies of ZnS NCs and then doping with Cu(I) ions (denoted as 5% Cu/ZnS'), and (iii) S-treatment of mesoporous Zn_{0.95}Cu_{0.05}S catalyst (denoted as Zn_{0.95}Cu_{0.05}S'). Interestingly, during the sulfur treatment of Zn_{0.95}Cu_{0.05}S NCAs, a fraction of S²⁻ ions are incorporated into the composite lattice, causing the partial oxidation of Cu(I) to Cu(II) (Eq. 4).



The presence of Cu(II) in the S-treated $\text{Zn}_{0.95}\text{Cu}_{0.05}\text{S}$ sample was evidenced by XPS spectroscopy, see Figure 18c.

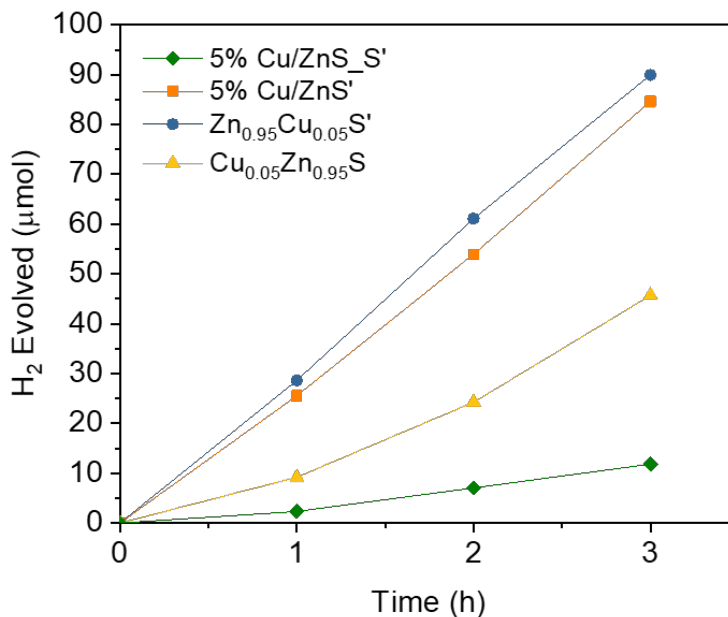


Figure 25: Time courses for photocatalytic H₂ production for different S-treated Zn_{0.95}Cu_{0.05}S NCAs. The H₂-production activity of Zn_{0.95}Cu_{0.05}S NCA catalyst is also given for comparison. The photocatalytic reactions were performed by suspending 20 mg of catalyst in 20 mL of water containing 0.25 M Na₂SO₃ and 0.35 M Na₂S, under $\lambda \geq 420$ nm light irradiation.

Figure 25 shows comparative results for the photocatalytic H₂-production activity of the S-treated catalysts. It can be seen that post-treatment of mesoporous ZnS and Cu-loaded ZnS structures with S²⁻ ions greatly improves the visible-light photocatalytic activity of the former catalyst. In particular, the mesoporous Zn_{0.95}Cu_{0.05}S' NC assemblies obtained after immersion of the ZnS and Zn_{0.95}Cu_{0.05}S NCAs in Na₂S solution achieve a hydrogen evolution rate of 28.2 and 30.0 μmol h⁻¹, respectively. In contrast, the composite sample prepared from S-treated ZnS NCs showed a significant lower activity, which corresponds to a H₂ evolution rate of 3.9 μmol h⁻¹ after 3 h of irradiation. Overall, the Zn_{0.95}Cu_{0.05}S'

NCAAs at 2 g L^{-1} concentration with $\text{S}^{2-}/\text{SO}_3^{2-}$ sacrificial electron donors achieve an H_2 -production rate of $\sim 1 \text{ mmol h}^{-1} \text{ g}_{\text{cat}}^{-1}$ in the initial 3 h. Assuming all incident photons are absorbed by the catalyst suspension, the apparent quantum efficiency (QE) for this reaction was measured to be 13.8% at $410 \pm 10 \text{ nm}$ light irradiation.

4.5 Recycling study of $\text{Zn}_{0.95}\text{Cu}_{0.05}\text{S}'$ NCAAs catalyst

The mesoporous assemblies of S-treated $\text{Zn}_{0.95}\text{Cu}_{0.05}\text{S}$ NCs also remain stable under the examined conditions. The stability of the $\text{Zn}_{0.95}\text{Cu}_{0.05}\text{S}'$ catalyst was studied by performing three consecutive 5-h photocatalytic cycles. After each catalytic cycle, the catalyst was isolated from the reaction mixture by centrifugation, washed with polysulfide solution to remove adsorbed sulfur species, and re-dispersed in a fresh reaction solution. Before photocatalytic reaction, the reaction cell was de-aerated by purging with argon to remove dissolved oxygen.

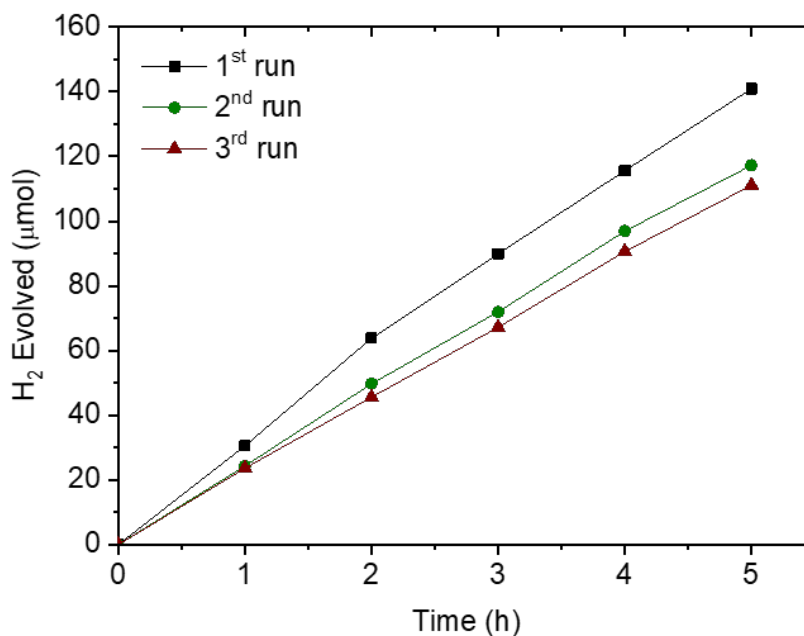


Figure 12: Recycling study of the $\text{Zn}_{0.95}\text{Cu}_{0.05}\text{S}'$ NCAAs catalyst. All the photocatalytic reactions were performed by suspending 20 mg of catalyst in 20 mL of water containing 0.25 M Na_2SO_3 and 0.35 M Na_2S , under $\lambda \geq 420 \text{ nm}$ light irradiation.

As shown in Figure 26, the $\text{Zn}_{0.95}\text{Cu}_{0.05}\text{S}'$ catalyst exhibits a quite stable H_2 evolution rate (within 5% tolerance) after the second catalytic run. A total H_2 amount of 0.37 mmol (~ 8.3 mL STP) was produced after 15 h of irradiation, corresponding to a H_2 evolution rate of $\sim 25 \mu\text{mol h}^{-1}$. The small decrease in H_2 evolution rate during the reuse tests is probably attributed to the mass loss of the catalyst during the recovery process. Although, minor photocorrosion of the $\text{Zn}_{0.95}\text{Cu}_{0.05}\text{S}'$ lattice during irradiation is a possible explanation for the lower activity.

The chemical composition and pore structure of the reused catalyst were investigated by EDS, XRD, XPS, and N_2 physisorption measurements (Figure 27). The EDS spectra showed a 48.1:5.2 Zn/Cu atomic, which corresponds to a ~ 5 mol% Cu content, in agreement with the composition of the fresh catalyst. The N_2 adsorption data indicated a surface area of $102 \text{ m}^2/\text{g}$, pore volume of $0.13 \text{ cm}^3/\text{g}$ and pore size of $\sim 4.6 \text{ nm}$; these values are very close to those of the fresh catalyst (see Table 2). Moreover, after catalysis the XRD pattern of $\text{Zn}_{0.95}\text{Cu}_{0.05}\text{S}'$ NCAs indicates preservation of the zinc-blende structure for the constituent ZnS NCs. In agreement to this, the XPS spectra of the reused catalyst also confirm the presence of ZnS and Cu_2S compounds in this sample (Figure 18).

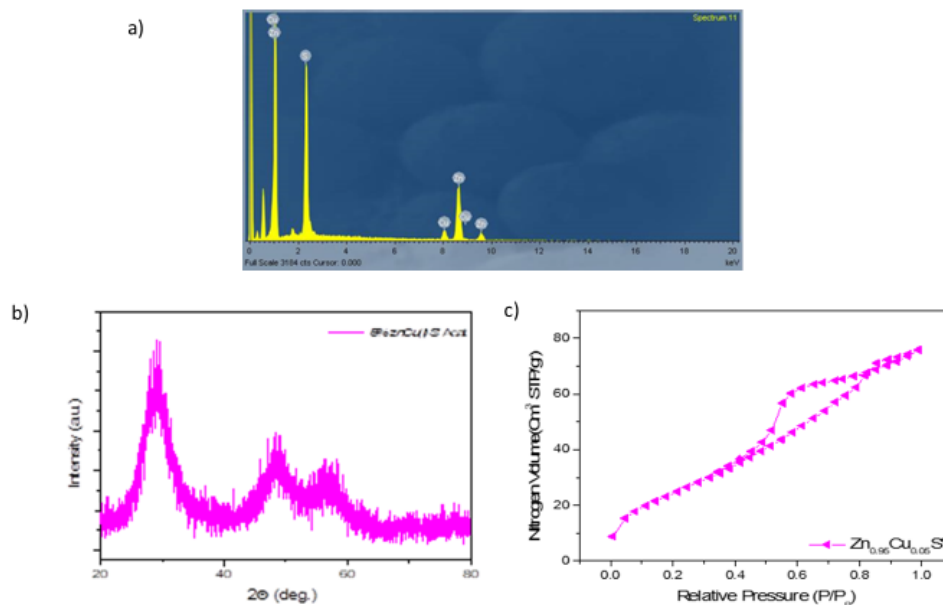


Figure 27: (a) EDS spectrum, (b) XRD pattern and (c) N_2 adsorption-desorption isotherms of mesoporous $\text{Zn}_{0.95}\text{Cu}_{0.05}\text{S}'$ NCAs after photocatalytic reaction.

4.6 Electrochemical properties

To elucidate the role of Cu_2S species in the H_2 -production activity of $\text{Zn}_{1-x}\text{Cu}_x\text{S}$ NCAs, we performed electrochemical impedance spectroscopy (EIS) studies. Figure 28 shows the $1/C^2$ versus applied voltage (V) curves and their corresponding linear fits for the mesoporous ZnS and $\text{Zn}_{1-x}\text{Cu}_x\text{S}$ NCA materials (drop-casted on FTO-coated glasses). The positive slopes of the $1/C^2 - V$ curves suggests n-type conductive, that is, electrons are the majority carriers. The Mott-Schottky plot analysis indicates that the flat-band potential (V_{FB}) of these samples shifts gradually toward more negative values, that is from -1.10 to -1.22 V (NHE, pH = 7), as the Cu content increases from 0 to 10 mol%. Furthermore, the charge donor density (N_d) of ZnS progressively decreases with increasing Cu content, as reflected by the increased slope of the $1/C^2$ versus V lines (see Table 4). On the other hand, treatment with sulfur seems to cause a positive shift in V_{FB} level (-1.16 V vs NHE, pH = 7) and increase in N_d concentration of the $\text{Zn}_{0.95}\text{Cu}_{0.05}\text{S}$ material.

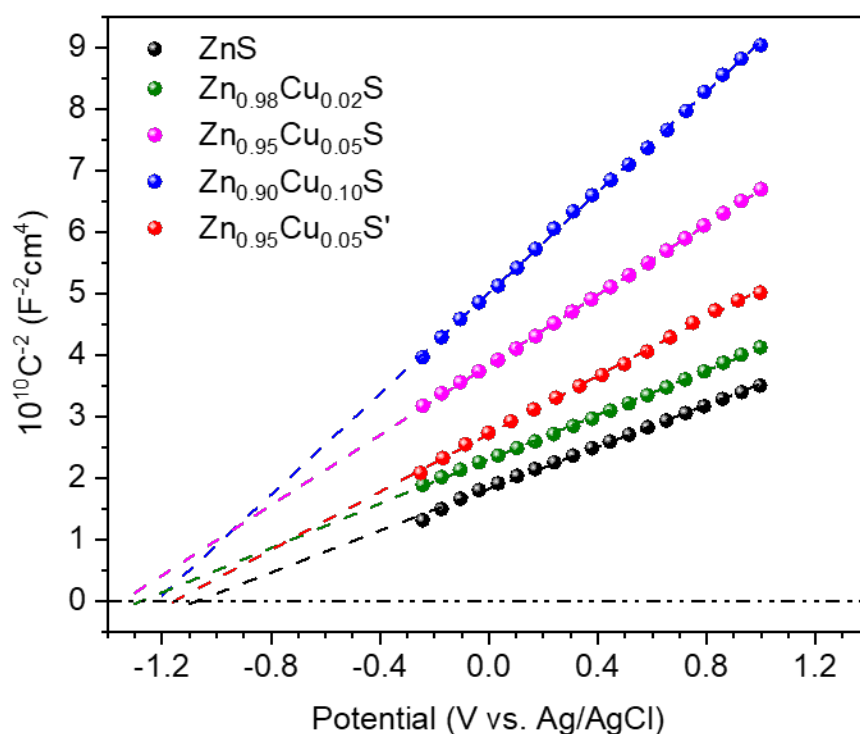


Figure 13 Mott-Schottky plots for mesoporous ZnS , $\text{Zn}_{1-x}\text{Cu}_x\text{S}$, and $\text{Zn}_{0.95}\text{Cu}_{0.05}\text{S}'$ NCA materials. The E_{FB} values were obtained from the intercepts of the extrapolated linear fits.

Based on the V_{FB} potentials and optical band gaps, as determined from UV-vis/NIR absorption spectra, the energy band diagram was constructed for each ZnS-based catalyst (Figure 29). Here we assumed that the flat band lies very close to the CB edge for heavily doped n-type ZnS. Therefore, the VB potential was obtained by adding to the V_{FB} potential the E_g value (Table 4).

Table 4. Electrochemical data (pH 7) for mesoporous ZnS, $Zn_{1-x}Cu_xS$ and $Zn_{0.95}Cu_{0.05}S'$ NCAs.

Sample	Flat Band, E_{FB} (V vs NHE)	VB potential (V vs NHE)	Slope ($F^{-2}cm^4/V$)	Donor density, N_d (cm^{-3})
ZnS	-0.89	2.99	1.70×10^{10}	9.32×10^{16}
$Zn_{0.98}Cu_{0.02}S$	-1.07	2.68	1.80×10^{10}	8.80×10^{16}
$Zn_{0.95}Cu_{0.05}S$	-1.14	2.18	2.85×10^{10}	5.56×10^{16}
$Zn_{0.90}Cu_{0.10}S$	-1.03	2.06	4.10×10^{10}	3.86×10^{16}
$Zn_{0.95}Cu_{0.05}S'$	-0.95	2.41	2.35×10^{10}	6.74×10^{16}

One likely reason for the observed negative shift in the V_{FB} potential and increase in N_d concentration in ZnS NCs with Cu addition is the formation of p-n junction created between ZnS and Cu_2S NCs; Cu_2S is a semiconductor with p-type conductivity [46]. In particular, given that the Fermi level of p-type Cu_2S (ca. 5.1 eV) [47] is positioned below the Fermi level of n-type ZnS (ca. 4.6-4.8 eV) [48], a built-in electrical potential should be established at the Cu_2S/ZnS interface. This thus results to an electron flow from the ZnS CB to the Cu_2S until the chemical potentials of two semiconductors reach equilibrium. The transfer of electrons may create a deformation of the band structure, that is, a depletion layer in ZnS and an accumulation layer in Cu_2S surface at the p-n Cu_2S/ZnS junction. Indeed, the formation of a depletion region in the ZnS phase coincides with the observed cathodic shift in V_{FB} s and decrease in N_d concentration with increasing Cu content in $Zn_{1-x}Cu_xS$ NCA materials, see Table 4.

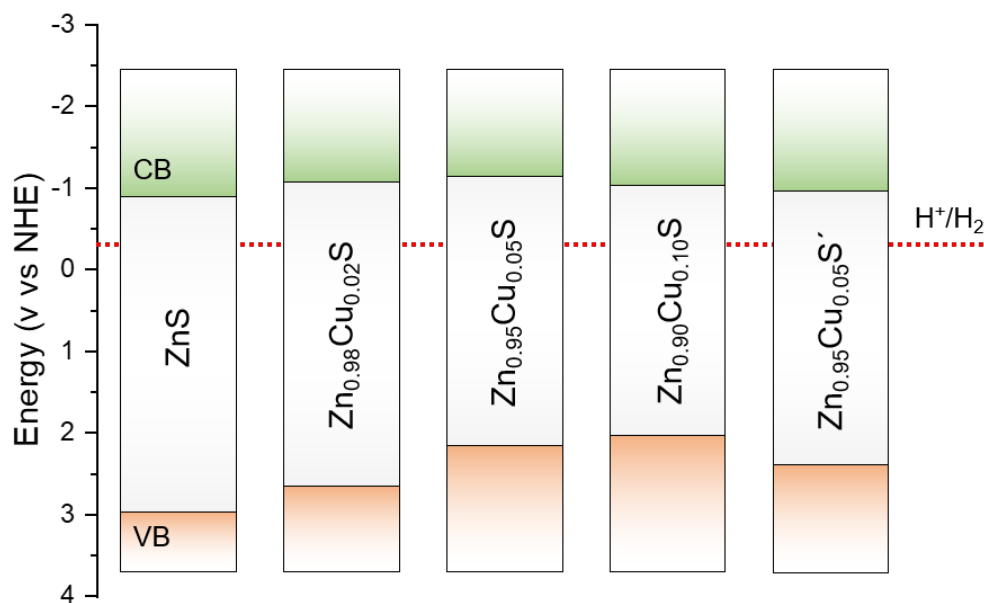


Figure 29: Energy band diagrams of the mesoporous ZnS, Zn_{1-x}Cu_xS, and Zn_{0.95}Cu_{0.05}S' NCAs (VB: valence band; CB: conduction band). The reduction potential of H⁺ to H₂ (-0.41 V vs NHE, pH = 7) is also given.

Overall the Cu₂S/ZnS junctions facilitate the spatial distribution of charge carriers through the appropriate alignment in the band-edge positions of the composites. This effect definitely has a great impact on the photocatalytic behavior of the Zn_{1-x}Cu_xS heterostructures. Briefly, under visible light irradiation, Cu₂S get excited and generate electron-hole pairs; Cu₂S has an energy band gap of 1.2–1.8 eV [49]. In addition, during the course of irradiation, a fraction of photoexcited electrons from the VB of ZnS may be transferred to the CuS clusters, causing their partial reduction to Cu₂S ($E^{\circ} = -0.91$ V vs NHE, pH = 7); the transition energy for this electronic excitation was estimated to be approximately 2.9 – 3.0 eV (~415–430 nm) and it is a viable option (Figure 30). Therefore, it is anticipated that the Cu₂S/CuS species will function as cocatalysts facilitating the charge separation through the interfacial electron transfer from ZnS to Cu₂S/CuS. Such an electron transfer mechanism may result in the reduction of CuS to Cu₂S. In agreement with this reaction scheme, the absence of Cu²⁺ ions in the regenerated Zn_{0.95}Cu_{0.05}S' catalyst was

confirmed by XPS spectroscopy (see Figure 18c). Moreover, the Cu₂S clusters could also promote the H₂ evolution reaction according to the following equations:



Meanwhile, the photoexcited holes in the VB of both ZnS and Cu₂S semiconductors can oxidize the sacrificial reagents (S²⁻/SO₃²⁻). Therefore, an efficient charge separation is successfully achieved through the p–n junctions of Cu₂S and ZnS NCs, leading to an enhanced photocatalytic H₂-production activity.

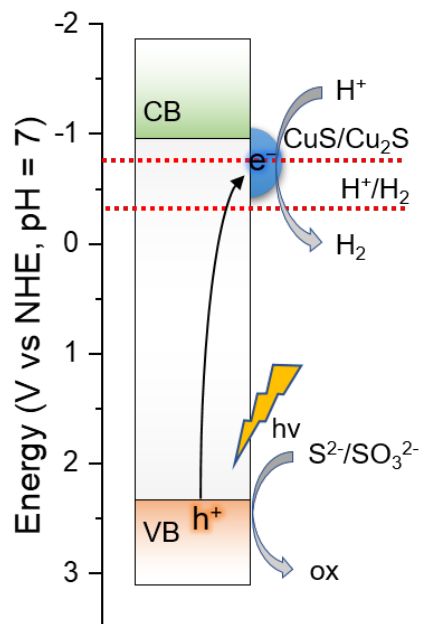


Figure 30: Schematic illustration for visible light induced interfacial electron transfer from the VB of ZnS to the CuS/Cu₂S clusters in Zn_{0.95}Cu_{0.05}S' NCA catalyst.

Conclusions

In summary, high-surface-area mesoporous networks of connected Cu-doped ZnS nanocrystals ($Zn_{1-x}Cu_xS$ NCAs; $x = 0.02, 0.05, 0.10$) have been successfully prepared via a polymer-templated aggregating assembly of colloidal ZnS nanocrystals, followed by chemical transformation into $Zn_{1-x}Cu_xS$ heterostructures. These materials show large internal BET surface area (ca. 142 – 314 m^2/g) and pore volume (ca. 0.14 – 0.28 cm^3/g), while the pore size distribution, as determined by NLDFT method, was found to be quite narrow with an average size of $\sim 4.4\text{--}4.8$ nm. Also, the pore walls of the obtained $Zn_{1-x}Cu_xS$ heterostructures consist of cubic zinc-blende ZnS and cubic chalcocite Cu_2S nanoparticles with high crystallinity, according to the X-ray diffraction (XRD), X-ray photoelectron spectroscopy (XPS), high-resolution TEM (HRTEM) and electron diffraction (SAED). The diffuse reflectance ultraviolet-visible/near-IR (UV-vis/NIR) spectroscopy results revealed that the $Zn_{1-x}Cu_xS$ NCAs have an optical absorption onset at $\sim 330\text{--}520$ nm, corresponding to an interband VB-to-CB electron transition of ~ 3.88 eV for pristine ZnS and $\sim 3.09\text{--}3.75$ eV for $Zn_{1-x}Cu_xS$ NCAs. Compared to ZnS, mesoporous $Zn_{1-x}Cu_xS$ heterostructures showed a considerable increase in H_2 production activity, indicating that the incorporated Cu_2S into the ZnS matrix have a prominent impact on the photocatalytic performance. The catalytic efficiency of $Zn_{1-x}Cu_xS$ NCAs increases with increasing the Cu content and reaches a maximum at 5 mol%; the $Zn_{0.95}Cu_{0.05}S$ NCAs catalyst give a H_2 evolution rate of 17.3 $\mu mol h^{-1}$, which is about 4.2 times higher than that of single-component ZnS sample. Indenting to further improve the photocatalytic performance of $Zn_{0.95}Cu_{0.05}S$, we produced a new modified $Zn_{0.95}Cu_{0.05}S'$ catalyst with controlled amount of S vacancies by sulfur treatment. Interestingly, we found that during this process, a fraction of S^{2-} ions are incorporated into the composite lattice, causing the partial oxidation of Cu(I) to Cu(II). This thus greatly improves the visible-light photocatalytic activity of the former catalyst. In particular, the mesoporous $Zn_{0.95}Cu_{0.05}S'$ NC assemblies obtained after immersion of the $Zn_{0.95}Cu_{0.05}S$ NCAs in Na_2S solution achieve a hydrogen evolution rate of 30.0 $\mu mol h^{-1}$, which is associated with an apparent QE of 13.8% at 410 ± 10 nm. The mesoporous network of S-treated $Zn_{0.95}Cu_{0.05}S$ NCs also remained stable under the

examined conditions. The chemical composition and pore structure of the reused catalyst were verified by EDS, XRD, XPS, and N₂ physisorption measurements.

References

- ¹ X. S. Zhao, *J. Mater. Chem.*, 2006, 16, 623.
- ² Y. Ren, *Chem. Soc. Rev.*, 2012, 2, 19.
- ³ D. Grosso, *Nature*, 1994, 317.
- ⁴ A. Fujishima, K. Honda, *Nature*, 1972, 238, 37.
- ⁵ R. Leary, A. Westwood, *Carbon*, 2011, 49, 741.
- ⁶ A. Taguchi, F. Schüth, *Micropor. Mesopor. Mater.*, 2005, 77, 1.
- ⁷ S. M. Zhu, H. S. Zhou, T. Miyoshi, M. Hibino, I. Honma, M. Ichihara, *Adv. Mater.*, 2004, 16, 2012.
- ⁸ A. Y. Khodakov, A. Griboval-Constant, R. Bechara, V. L. Zholobenko, *J. Catal.*, 2002, 206, 230.
- ⁹ X. Wang, X. Bu, P. Feng, in “*Encyclopedia of Inorganic Chemistry: Porous Inorganic Materials*”, John Wiley & Sons, 2006.
- ¹⁰ S. J. Gregg, K. S. W. Sing, in “*Adsorption, Surface Area and Porosity*”, Academic Press, San Diego, 1982.
- ¹¹ S. Polarz, B. Smarsly, *J. Nanosci. Nanotechnol.*, 2002, 2, 581.
- ¹² D. C. Bradley, E. Pitzer, W. J. Koves, *Symp. Ser.*, 1988, 411, 398.
- ¹³ R. C. Mehrotra, *J. Non-Cryst. Solids*, 1992, 145, 1.
- ¹⁴ J. F. Brinker, G. W. Scherer in “*Sol-Gel Science: The Physics and Chemistry of Sol-Gel Processing*”, Academic Press, Boston, 1990.
- ¹⁵ G. Leofanti, G. Tozzola, M. Padovan, G. Petrini, S. Bordiga, A. Zecchina, *Catal. Today*, 1997, 34, 307.
- ¹⁶ H. Q. Lijia Pan, *Int. J. Mol. Sci.*, 2010, 2638.
- ¹⁷ P. D. Yang, D. Y. Zhao, D. I. Margolese, B. F. Chmelka, G. D. Stucky, 1998, 396, 152.
- ¹⁸ M. Janicke, D. Kumar, G. D. Stucky, B. F. Chmelka, *Stud. Surf. Sci. Catal.* 1994, 84, 243.
- ¹⁹ J.S. Beck, J.C. Vartuli, W.J. Roth, *J. Am. Chem. Soc.* 1992, 114, 10834.
- ²⁰ S. C. Warren, L. C. Messina, L. S. Slaughter, M. Kamperman, Q. Zhou, S. Gruner, F. J. DiSalvo, U. Wiesner, *Science*, 2008, 320, 1748.

-
- ²¹ I. T. Papadas, I. Vamvasakis, I. Tamiolakis, G. S Armatas, *Chem. Mater.*, 2016, 28, 2886.
- ²² I. T. Papadas, S. S. Kota, M. G. Kanatzidis, G. S Armatas, *Nanoscale*, 2015, 7, 5737.
- ²³ I. T. Papadas, S. Fountoulaki, I. N. Lykakis, G. S. Armatas, *Chem. A Eur. J.*, 2016, 22, 4600.
- ²⁴ M.R. Hoffmann, S. T. Martin et al, *Chem. Rev.*, 1995, 95, 69.
- ²⁵ M. R. Gholipour, C.-T. Dinh, F. Béland, T.-O. Do, *Nanoscale*, 2015, 7, 8187,
- ²⁶ A. Kudo, Y. Miseki, *Chem. Soc. Rev.*, 2009 , 38 , 253.
- ²⁷ X. Li, J. Yu, J. Low, Y. Fang, J. Xiao, X. Chen, *J. Mater. Chem. A*, 2015, 3, 2485.
- ²⁸ S. Brunauer, L. S. Deming, W. E. Deming, *J. Am. Chem. Soc.*, 1940, 62, 1723.
- ²⁹ P. I. Ravikovitch, D. Wei, W. T. Chueh, G. L. Haller, A. V. Neimark, *J. Phys. Chem. B*, 1997, 101, 3671.
- ³⁰ S. W. Gaarenstroom, *J. Chem. Phys.*, 1977, 67, 3500.
- ³¹ P. Kubelka, *J. Opt. Soc. Am.*, 1948, 38, 448.
- ³² J. Tauc, in "Optical Properties of Amorphous Semiconductors. In Amorphous and Liquid Semiconductors", Plenum Press, New York, 1974; pp 159-220.
- ³³ Lange's Handbook, pp. 8-6 to 8-11; L.G. Sillen and A.E. Martell, "Stability Constants of Metal-Ion Complexes," The Chemical Society, London, 1964 (Special Publ. No. 17).
- ³⁴ S. W. Gaarenstroom, N. Winograd, *J. Chem. Phys.*, 1977, 67, 3500.
- ³⁵ R. Islam, D. R. Rao, *J. Electron Spectros. Relat. Phenomena*, 1996, 81, 69.
- ³⁶ E. Agostinelli, C. Battistoni, D. Fiorani, G. Mattogno, M. Nogues, *J. Phys. Chem., Solids*, 1989, 50, 269.
- ³⁷ L. S. Dake, D. R. Baer, J. M. Zachara, *Surf. Interface Anal.*, 1989, 14, 71.
- ³⁸ Y. J. Lu, J. Jia, J. H. Chin., *Chem. Lett.*, 2014, 25, 1473.
- ³⁹ I. Nakai, Y. Sugitani, K. Nagashima, Y. Niwa, *J. Inorg. Nucl. Chem.*, 1978, 40, 789.
- ⁴⁰ M. C. Biesinger, *Surf. Interface Anal.*, 2017, 49, 1325.
- ⁴¹ P. Liu, E. J. M. Hensen, *J. Am. Chem. Soc.*, 2013, 135, 14032.
- ⁴² F. Severino, J. L. Brito, J. Laine, J. L. G. Fierro, A. L. Agudo, *J. Catal.*, 1998, 177, 82.
- ⁴³ A. B. F. Martinson, S. C. Riha, E. Thimsen, J. W. Elam, M. J. Pellin, *Energy Environ. Sci.*, 2013, 6, 1868.

-
- ⁴⁴ M. Thommes, *Chem. Ing. Tech.*, 2010, 82, 1059.
- ⁴⁵ K. Sooklal, B. S. Cullumn, S. M. Angel, C. J. Murphy, *J. Phys. Chem.*, 1996, 100, 4551.
- ⁴⁶ Z. C. Wu, C. Pan, Z. Y. Yao, Q. R. Zhao, Y. Xie, *Cryst. Growth Des.*, 2006, 6, 1717.
- ⁴⁷ S. Gupta, Y. Batra, B. R. Mehta, V. R. Satsangi, *Nanotechnology*, 2013, 24, 255703.
- ⁴⁸ F. Mesa, W. Chamorro, W. Vallejo, R. Baier, *J. Nanotechnol.*, 2012, 3, 277.
- ⁴⁹ M. Ramya, S. Ganesan, *Iran J. Mater. Sci. Eng.*, 2011, 8, 34.